Geochemistry, Geophysics, Geosystems

RESEARCH ARTICLE
10.1029/2019GC008632

Long-Term Storage and Age-Biased Export of Fluvial Organic Carbon: Field Evidence From West Iceland

Mark A. Torres[1], **Preston C. Kemeny**[2], **Michael P. Lamb**[2], **Trevor L. Cole**[1], **and Woodward W. Fischer**[2]

[1]Department of Earth, Environmental, and Planetary Sciences, Rice University, Houston, TX, USA, [2]Division of Geological and Planetary Sciences, California Institute of Technology, Pasadena, CA, USA

Key Points:
- Bulk radiocarbon measurements of riverine organic matter revealed millennial-scale aging during sediment storage in Iceland
- XANES identifies interparticle diversity in S redox states indicative of organic matter with multiple origins and/or diagenetic histories
- Physical storage dynamics in river floodplains may influence the carbon cycle

Supporting Information:
- Supporting Information S1
- Data Set SI

Correspondence to:
M. Torres,
mt61@rice.edu

Citation:
Torres, M. A., Kemeny, P. C., Lamb, M. P., Cole, T. L., & Fischer, W. W. (2020). Long-term storage and age-biased export of fluvial organic carbon: Field evidence from West Iceland. *Geochemistry, Geophysics, Geosystems*, *21*, e2019GC008632. https://doi.org/10.1029/2019GC008632

Received 23 AUG 2019
Accepted 14 DEC 2019
Accepted article online 15 MAR 2020

Abstract Terrestrial organic carbon (OC) plays an important role in the carbon cycle, but questions remain regarding the controls and timescale(s) over which atmospheric CO_2 remains sequestered as particulate OC (POC). Motivated by observations that terrestrial POC is physically stored within soils and other shallow sedimentary deposits, we examined the role that sediment storage plays in the terrestrial OC cycle. Specifically, we tested the hypothesis that sediment storage impacts the age of terrestrial POC. We focused on the Efri Haukadalsá River catchment in Iceland as it lacks ancient sedimentary bedrock that would otherwise bias radiocarbon-based determinations of POC storage duration by supplying pre-aged "petrogenic" POC.

Our radiocarbon measurements of riverine suspended sediments and deposits implicated millennial-scale storage times. Comparison between the sample types (suspended and deposits) suggested an age offset between transported (suspended sediments) and stored (deposits) POC at the time of sampling, which is predicted by theory for the sediment age distribution in floodplains. We also observed that POC in suspended sediments is younger than the predicted mean storage duration generated from independent geomorphological data, which suggested an additional role for OC cycling. Consistent with this, we observed interparticle heterogeneity in the composition of POC by imaging our samples at the microscale using X-ray absorption spectroscopy. Specifically, we found that particles within individual samples differed in their sulfur oxidation state, which is indicative of multiple origins and/or diagenetic histories. Altogether, our results support recent coupled sediment storage and OC cycling models and indicate that the physical drivers of sediment storage are important factors controlling the cadence of carbon cycling.

1. Introduction

Terrestrial organic carbon (OC) present in the biosphere, soils, and other shallow sedimentary deposits represents an enormous carbon reservoir that is currently much larger than the mass of CO_2 present in the atmosphere (pre-industrial values of ~4,200 vs. 589 PgC; Pachauri et al., 2014). Fluxes associated with the terrestrial OC reservoir are dynamic from seasonal to geologic timescales (France-Lanord & Derry, 1997; Keeling, 1960; Keeling & Shertz, 1992) and thus may meaningfully modulate atmospheric CO_2 levels (Ciais et al., 2012; He et al., 2016; Stallard, 1998). However, to evaluate the exact role of OC in the global carbon cycle and climate system, we require constraints on the duration over which atmospheric CO_2 remains sequestered as OC and the environmental influences on these timescales.

Existing paradigms for the terrestrial OC cycle focus on how biological and geochemical factors influence the duration of OC storage by modulating the relative rates of OC production and consumption (Raich & Schlesinger, 1992; Schmidt et al., 2011). However, the observation that a majority of terrestrial OC is physically stored as particulate OC (POC) within sedimentary deposits (Cierjacks et al., 2010; Doetterl et al., 2016; Hoffmann et al., 2009; Lininger et al., 2019; Pachauri et al., 2014; Stallard, 1998; Sutfin et al., 2016, 2017; Wohl et al., 2012, 2017) implies that sediment storage and transport processes should also play an important modulating role. For instance, estimates of the duration of sediment storage in terrestrial systems (10^3 to 5×10^5 years; Blöthe & Korup, 2013; Granet et al., 2010; Li et al., 2016; Wittmann et al., 2015) are of similar order to the inferred timescales of terrestrial POC storage (greater than 10^3 years; Galy & Eglinton, 2011; Tao et al., 2015; Torn et al., 1997). Moreover, the results of a large body of biogeochemical studies support a

close physical association between OC and sedimentary particles (Hemingway et al., 2019; Kennedy et al., 2002; Lalonde et al., 2012; Mayer, 1994).

Sediment, and the POC it contains, is transiently stored on landscapes in a variety of landforms including on hillslopes and in fluvial deposits. Sediment transport across continents occurs primarily by rivers, and storage times in fluvial deposits typically exceed hillslope storage times for pan-continental drainage basins (Dosseto et al., 2006; Li et al., 2016). Physical models of fluvial transport predict complex sediment storage time distributions due to the lateral migration of river channels across their floodplains with time. Steady-state storage time distributions are predicted to be heavy tailed (e.g., power law) due to the preferential removal of young deposits close to the channel, which requires that the older deposits are stored for longer than expected relative to models without age-selective entrainment (Bolin & Rodhe, 1973; Bradley & Tucker, 2013; Torres et al., 2017). Inasmuch as POC transport is governed by the same physics (i.e., young deposits with young OC are preferentially reworked), OC age distributions may also be heavy tailed. By coupling a morphodynamic sediment storage model (Howard & Knutson, 1984; Limaye & Lamb, 2013) with an OC cycling model (Jenny et al., 1949), Torres et al. (2017) showed that the impact of sediment storage dynamics on POC storage remains even with realistic levels of OC cycling, which act to decouple sediment and OC ages. If this inference is correct, riverine transport dynamics would influence how C is sequestered or released in response to environmental or anthropogenic changes, as well as how environmental proxy records get preserved in sediments (Douglas et al., 2014; French et al., 2018; Torres et al., 2017). However, whether or not the terrestrial OC cycle is influenced by age-biased sediment entrainment/storage remains to be evaluated with field data.

Prior work (Bradley & Tucker, 2013; Malmon et al., 2003; Torres et al., 2017) illustrated that a heavy-tailed storage time distribution can result from the dynamics of fluvial lateral migration alone. However, cycles of channel aggradation and incision may create similar age distributions (Ganti et al., 2011). For example, the burial of deposits (and their OC) beneath the depth of channel reworking and exposure to dioxygen may occur for long periods of time, only for these deposits to later be re-exposed and exported. This sort of timescale dependence in net sediment accumulation is widespread in sedimentary systems (Sadler, 1981) and thus may be an important component of sediment (and POC) age distributions. Importantly, two key features of sediment transport and accumulation in fluvial settings—lateral channel migration and channel cut and fill cycles—provide mechanisms that might give rise to heavy-tailed storage timescales, and this in turn may set the pace of OC storage and cycling in terrestrial landscapes.

Testing for heavy-tailed storage by characterizing the full age distribution of OC is challenging due to spatiotemporal heterogeneity in sediment entrainment, deposition, and mixing as well as nonlinearity and nonuniqueness in proxies for OC ages. Transport models with age-selective entrainment predict an age offset between the OC exported from the catchment and the OC remaining stored within the floodplain (Bolin & Rodhe, 1973; Bradley & Tucker, 2013; Torres et al., 2017). Without age-selective transport, there should not be a difference in the age distribution of stored versus exported OC even if the kinetics of OC cycling have heavy-tailed properties (e.g., Middelburg, 1989) since the sampling from this reservoir of stored OC would not be biased (Bolin & Rodhe, 1973; Bradley & Tucker, 2013). In this way, the age offset between transported and stored sediments can serve as a marker of the role of age-selective transport and storage in setting the lifetime of terrestrial POC.

Terrestrial POC storage times can, in principle, be quantified using radiocarbon (^{14}C; half-life = 5,730 years). However, interpreting the ^{14}C content of bulk POC in terms of a storage time can be complicated due to the inheritance of radiocarbon-dead "petrogenic" OC in particles eroded from ancient sedimentary rocks in the catchment (Bouchez et al., 2010; Galy et al., 2008; Masiello & Druffel, 2001). So, despite important previous work on the POC content of floodplains (Cierjacks et al., 2010; Hoffmann et al., 2009; Lininger et al., 2019; Sutfin et al., 2016, Sutfin & Wohl, 2017; Wohl et al., 2012, 2017), these works cannot be used to test for long-term storage and/or age-selective entrainment because they did not account for petrogenic carbon. In one effort to circumvent this complication, several studies of terrestrial POC storage times (Galy & Eglinton, 2011; Martin et al., 2013; Tao et al., 2015) analyzed the ^{14}C content of select "biomarker" compounds. These biomarker compounds are helpful because they constrain the provenance of specific biological materials, but they also typically represent <1% of the total mass of POC in a given sample. Moreover, at a single field site, different types of biomarker compounds (e.g., lignin phenols, fatty acids, or alkanes) can yield different

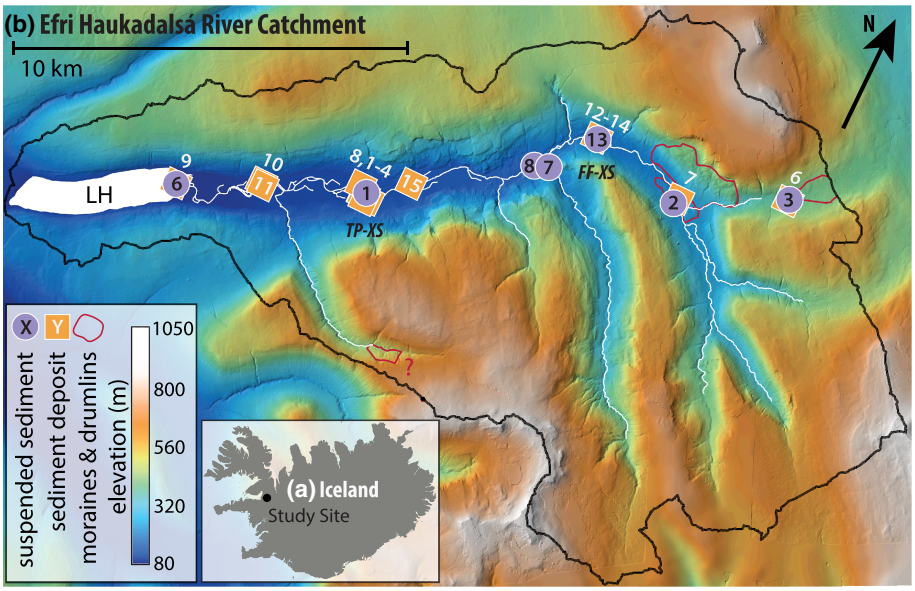

Figure 1. (a) Location of the Efri Haukadalsá study site within Iceland. (b) Topography and sampling locations within the Efri Haukadalsá River catchment. Squares denote sediment sampling locations (LHSS), and circles denote water sampling locations (LHWS). The red outlines indicate areas determined to contain glacial sediments (moraines and drumlins). The black outline shows the watershed area for Lake Haukadalsvatn. The locations of the two field measured cross sections are indicated as "TP-XS" and "FF-XS" (see supporting information Figure S3).

apparent ages (Martin et al., 2013; Tao et al., 2015). Altogether, these observations underscore the current challenges associated with inferring POC storage times in river catchments containing sedimentary bedrock.

To test hypotheses about the aging of POC during fluvial storage, we studied carbon cycling and sediment storage in the Efri Haukadalsá River catchment in West Iceland. The basaltic bedrock of Iceland is effectively devoid of POC and facilitates the use of the ^{14}C content of POC as tracer of the timescale(s) of POC storage in fluvial systems (cf. Bouchez et al., 2010; Galy et al., 2008; Masiello & Druffel, 2001). This approach allows one to more directly assess aging of OC without extrapolating from biomarker measurements or correcting for contributions from petrogenic OC. In addition to documenting millennial-scale POC storage times, we also compared the ^{14}C contents of POC in fluvial deposits versus riverine suspended sediments to identify evidence for age-selective POC entrainment. While our data supported the hypothesis that "young" POC sourced from recent deposits is preferentially exported from the catchment, the apparent age of exported POC is less than expected from independent estimates we made of the duration of sediment storage. This discrepancy may result from the continued production and consumption of OC during floodplain storage. To further evaluate this hypothesis, we made measurements of OC molecular compositions based on sulfur K-edge X-ray Adsorption Near Edge Spectroscopy (XANES). These data show a diversity of electronic structure and redox states of S moieties in the POC, and, importantly, that individual particles within a sample differ strongly in their mean S oxidation state relative to other particles in the same sample. This latter observation is indicative of a range of particle sources and/or diagenetic histories, which is consistent with a combined role of storage and OC cycling in setting POC compositions and age distributions.

2. Materials and Methods

2.1. Study Site

The Efri Haukadalsá River in West Iceland flows through a glacially carved valley into Lake Haukadalsvatn (Figures 1 and 2a; catchment area = 170 km^2). Measured at the outlet of the lake, the mean annual water discharge of the Efri Haukadalsá River is 13.4 $m^3\ s^{-1}$ (Icelandic Meteorological Office). Based on a nearby weather station with 25 years of measurements (Ásgarður station; ~21 km from the inlet of Lake Haukadalsvatn), the mean annual temperature of the region is 3.8°C. The average temperature during December, January, February, and March is below 0°C. The hottest month is July, which reaches an average temperature of 10.8°C.

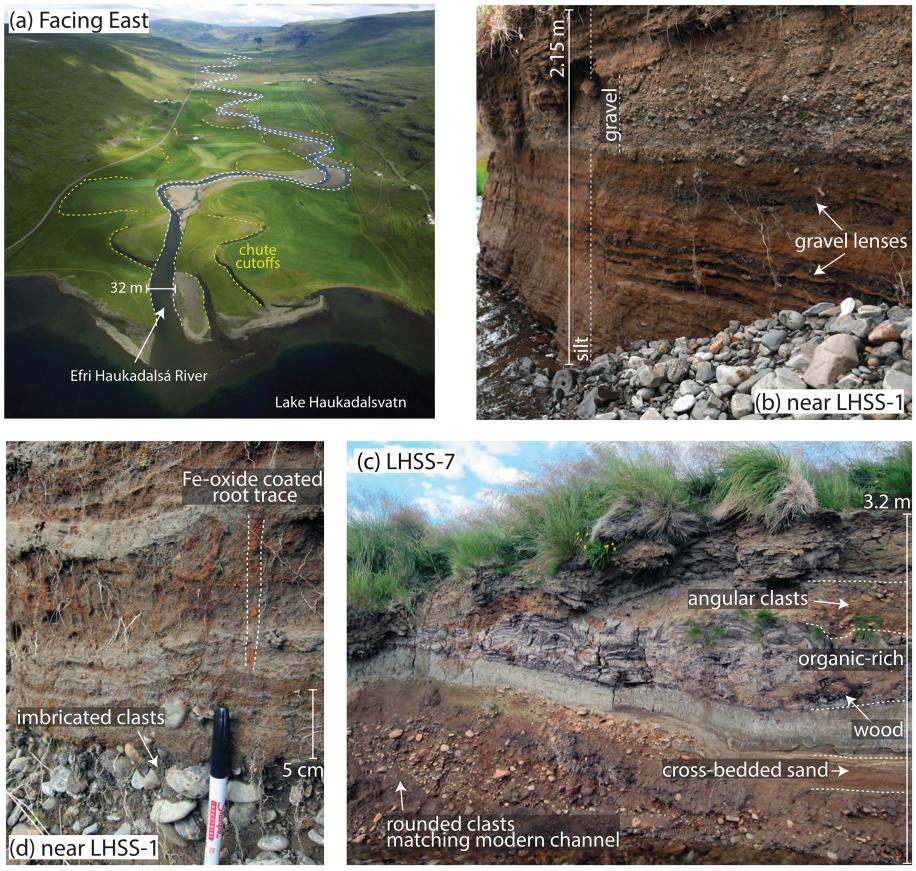

Figure 2. (a) East facing aerial image of the study catchment. The flow of the Efri Haukadalsá River is toward Lake Haukadalsvatn. The active channel of the Efri Haukadalsá River is outlined with white dashed lines, and reaches abandoned via chute cutoffs are outlined with yellow dashed lines. (b) Image of floodplain sediments exposed in a cut bank near LHSS-1 (Figure 1) showing the mixture of silt and gravel deposits characteristic of much of the valley. (c) Close-up of a deposit near LHSS-1 showing the iron oxide coated root casts that generate a mottled texture in the sand and silt deposits. (d) Image of floodplain sediment exposed in a cut bank at the LHSS-7 sampling site. The image shows meter-scale variability in deposit geometry as well as the locations of various depth horizons discussed in the text (i.e., the organic-rich horizon and the deposit of angular clasts).

Human settlement of the Efri Haukadalsá River valley began in 10th century, and the region has been continuously, but sparsely, occupied since (notable inhabitants are thought to include Erik the Red and his son Leif Erikson; Ólafsson, 1998). Historical accounts and site names describe the valley as originally being forested. At present (and since before the 1700s), the valley is not forested and is instead occupied by grasses and sedges (Geirsdóttir et al., 2009).

The channel of Efri Haukadalsá River migrates laterally across the alluviated valley by meandering and chute cutoffs (Figures 2a and 6a–6c). Time series of Landsat images document multiple chute cutoffs since 1987, indicating that channel migration is currently active and dynamic over decadal timescales.

An existing sediment core from Lake Haukadalsvatn provides constraints on the history of the Efri Haukadalsá River valley and its relationship to the OC cycle (Geirsdóttir et al., 2009). Collected near the deepest portion of the lake, the 30 m sediment core captures a complete section as it is bounded by bedrock at its bottom (Figure 3b). Fine-grained sediments containing drop stones and mollusc shells at the base of the core record marine conditions when the upstream river catchment was glaciated (Geirsdóttir et al., 2009). Deglaciation around 10 ka followed by isostatic rebound drove a shift from marine toward lacustrine sedimentation of laminated muds and silts (Geirsdóttir et al., 2009).

Based on C to N ratios and $\delta^{13}C$, Geirsdóttir et al. (2009) interpreted the POC in the lacustrine portion of the core to derive primarily from the upstream river catchment. Intriguingly, base-extractable POC consistently has a lower ^{14}C content than would be expected based on the depositional age derived from

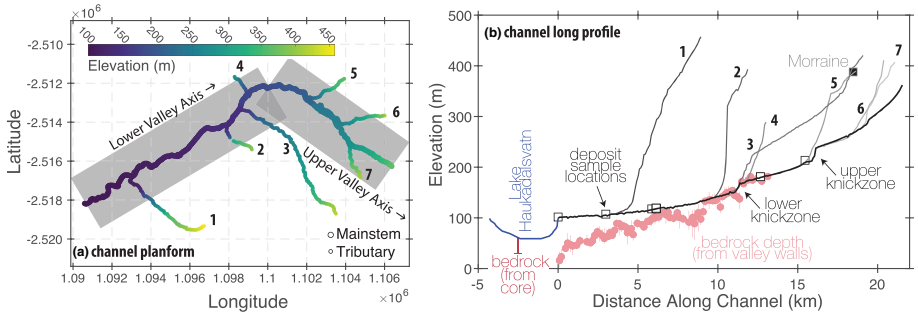

Figure 3. River channel topography. (a) Channel planform extracted using GRASS GIS flow routing algorithms and the PRC DEM. The larger points correspond to the mainstem while the smaller points denote tributaries (numbered according to distance upstream). The elevations of all of the channels are given by the color scale. The gray boxes represent the locations and orientations of the cross sections used to quantify the amount of alluvial cover and depth to bedrock (section 2.4). (b) The long profile of the Efri Haukadalsá River (black) and major tributaries (gray; same numbering as in panel (a)). The blue line shows the bathymetry of Lake Haukadalsvatn. The gray squares show the locations of deposit sampling sites relative to the mainstem. The pink circles show the estimates of the maximum depth to bedrock derived from the analysis of topographic cross sections (see Figure 4a). The uncertainty bounds show the full range in depths predicted by fitting different portions of the valley walls. For comparison to the topographic estimates of depth to bedrock, we show the approximate location of the sediment core described in Geirsdóttir et al. (2009) (pink line) and the measured depth to bedrock from drilling.

tephrachronology (Geirsdóttir et al., 2009). This observation suggests substantial pre-aging of POC within the Efri Haukadalsá River catchment prior to its delivery to Lake Haukadalsvatn. In their original discussion, Geirsdóttir et al. (2009) interpreted the changing magnitude of OC pre-aging, which roughly increases toward the present, to result from increases in wind-derived sediment inputs. Here, we revisit this observation of OC pre-aging in the Efri Haukadalsá River system by directly characterizing the radiocarbon content of POC in fluvial deposits and riverine suspended sediments.

In summary, the Efri Haukadalsá River valley appears to be a glacial overdeepened valley bounded by a bedrock ridge on the downstream end of the lake (Figures 1 and 3b). Following deglaciation, it is likely that the lake has been filling with fluvially transported sediment derived from the catchment as evidenced by the valley width spanning delta at the upstream margin of the lake (Figure 2a). Fluvio-deltaic systems aggrade as they prograde to maintain the necessary transport slope (Muto & Steel, 1992). In addition, the river is meandering, and the floodplain contains evidence of past channel courses and cutoff bends (Figure 2a), suggesting that the river actively distributes sediment across the floodplain through lateral migration. Thus, since deglaciation, sediment appears to be stored in the valley by two main mechanisms: lateral migration and overbank deposition that spread sediment laterally across the valley, and aggradation in response to delta-front progradation into Lake Haukadalsvatn that is filling the glacial overdeepend valley.

2.2. Field Sample Collection

Field samples of sediment deposits and riverine suspended sediments were collected in August 2016 over a 2 week period. Limited access within the catchment influenced the locations of the specific sampling localities. Depending upon their location, the sediment deposits were sampled in one of the two ways. When exposed at river cut banks, the surfaces of sediment deposits were excavated with a trowel before sampling. For deposits without a surface exposure, samples were retrieved using a steel hand auger. In all cases, variations in deposit grain size and sedimentary structures with depth were described in the field, and a sample from each discernible unit was collected into a polyethylene Whirl-Pak bag. After collection, the river deposit samples were stored frozen. In total, 42 deposit samples were collected from 12 sites, which are identified with the prefix "LHSS" (Figure 1).

Samples of the suspended sediments in rivers were collected using an acrylic 8.2 L Van Dorn-type sampler (Wildco). The sampler was positioned in the channel thalweg and triggered by hand. Due to the low suspended sediment concentrations at the time of sampling, multiple casts were collected for each sample and stored in separate 10 L polyethylene bags. Within 24 hr of collection, the samples were filtered through pre-combusted 142-mm-diameter glass fiber filters (Sterilitech; nominal pore size of 0.3 μm) using a custom-built pressure filtration unit made from stainless steel and Teflon parts. For each sample, all suspended sediment was collected onto a single filter. When necessary, insect larvae and large plant debris were

manually removed from the filter surface using clean stainless steel tweezers. The sediment-laden filters were placed into sterile plastic petri dishes and stored frozen. In total, nine suspended sediment samples were collected from eight sites indicated by the prefix "LHWS" (Figure 1). Site LHWS-1 was sampled twice to capture runoff from a storm event that occurred during our fieldwork.

2.3. Laboratory Analyses

2.3.1. Carbon Concentration and Isotopic Measurements

The frozen sediment deposit samples were freeze-dried and then ground to a fine powder using an agate mortar and pestle. Subsamples of the frozen suspended sediment-laden filters were collected using a metal hole punch (5 mm diameter for concentration and stable isotopic ratios; 50 mm diameter for radiocarbon). The filter subsamples were dried overnight in pre-combusted glass petri dishes at 60°C in an oven.

To determine bulk carbon concentrations, 1 to 2 mg of each ground deposit sample or 1 to 3 filter punches (5 mm) were weighed into silver capsules and analyzed using a Costech Elemental Analyzer with either a flame ionization detector (at the University of Southern California) or a Thermo Delta V mass spectrometer running in continuous-flow mode (at Caltech). When analyzed using the mass spectrometer, the carbon isotopic ratio ($\delta^{13}C$) of liberated CO_2 was also determined. The concentrations and stable isotopic ratios were standardized using two reference materials (NIST Sucrose 8542 and IVA Urea 33802174) run after every five samples. In total, 34 samples were measured for bulk C concentrations (8 filters and 26 deposits). We note that we did not pre-treat the concentration samples with acid under the assumption that the sediments contained little to no particulate inorganic carbon (PIC; see below).

The OC concentrations of the suspended sediments (in units of mass of C per mass of sediment) could only be estimated for two samples due to methodological issues. Specifically, since the filters were not pre-weighted, the weight of sediment was calculated by weighing an equivalently sized punch of an unused filter and subtracting it from the total weight from each sediment-laden filter. For all but two samples, this approach yielded negative concentrations presumably due to variability in the weight of each filter punch and overall low particle masses.

To determine the radiocarbon (^{14}C) content of POC, aliquots of ground deposit samples and filter subsamples were measured at the National Ocean Sciences Accelerator Mass Spectrometry Facility (NOSAMS). Before analysis, the samples were exposed to HCl fumes following established NOSAMS protocols for removing PIC. While we did not expect the samples to have significant amounts of PIC, even trace amounts of any ^{14}C-dead material could seriously bias the radiocarbon measurement, and carbonate minerals are known to occur as alteration products in some Icelandic basalts (Mehegan et al., 1982; Muehlenbachs et al., 1974). To evaluate the discrepancy in the sample preparation method between our concentration, stable isotopic, and radiocarbon analyses, splits of the exact gas used for ^{14}C were also analyzed for $\delta^{13}C$ at NOSAMS. In total, we measured 34 radiocarbon samples (8 filters, 25 deposits, and 1 wood sample). The measurements of radiocarbon contents are expressed as the Fraction Modern (*Fm*), which is defined as

$$Fm = \frac{\frac{^{14}C}{^{12}C}_{\text{sample}}}{\frac{^{14}C}{^{12}C}_{\text{standard}}} \quad (1)$$

where both the standard and sample ratios have been adjusted for mass-dependent stable isotopic fractionation based on the measured ratio of ^{13}C to ^{12}C.

Comparison between the $\delta^{13}C$ measured with and without acid treatment reveals a significant discrepancy where the acidified samples are more variable and, typically, have lower $\delta^{13}C$ values (Figure S1). In principle, this offset could be due to the presence of PIC in the un-acidified samples and its removal upon sample acidification. So, as a check on our assumption of a lack of PIC, two bedload sediment samples (LHWS-1 and LHWS-6) were dry-sieved into five grain size fractions using 500, 212, 90, 45, and 7 μm pore-size sieves. Bedload samples were selected as they are typically less chemically altered and, as a result, may better preserve reactive phases like carbonates. The sieved bedload samples were subsequently ground and pelletized with a hydraulic press for the determination of major element concentrations (Ca, Si, and C) using a field emission Electron Probe MicroAnalyzer (JEOL JXA 8530F Hyperprobe) at Rice University equipped with a field emission assisted thermo-ionic (Schottky) emitter and five wavelength dispersive spectrometers.

The wavelength dispersive spectrometer quantitative elemental maps were acquired at 15 kV accelerating voltage, 50 nA beam current, using stage mode with 10 ms dwell time. Our analysis utilized an electron

beam width of 300 nm, and, for samples LHWS-1 and LHWS-6, the scanned areas are 900 by 900 and 945 by 725 μm, respectively. The maps were adjusted for dead time correction, and the following standards were employed for quantification of elements using the Kα X-ray line: olivine (Fo93) for Si, diopside for Ca, and graphite for C. Additional details of this analysis are provided in the supporting information.

To test for the presence of $CaCO_3$ in each sample, we isolated analysis spots that returned C to Ca ratios within 5% of 0.3 (i.e., the mass ratio in $CaCO_3$). These spots have high Si concentrations similar to the bulk sample, are present at the boundaries between OC and silicate particles, and make up less than 5% of sampled area (Figure S2). Therefore, we conclude that carbonate phases are not present at a sufficient concentration in our samples to explain the isotopic data, and, as a result, we assume that the $\delta^{13}C$ offset between acidified and un-acidified samples results from the breakdown of reactive functional groups present in natural organic matter as observed in other studies (e.g., Bao et al., 2019). For internal consistency as well as to match most previously published work on riverine POC where acidification was utilized to remove PIC, we report the $\delta^{13}C$ values measured by NOSAMS (i.e., the acid-treated samples) in the main text as they represent the same aliquot of CO_2 used for radiocarbon determination.

2.3.2. X-ray Absorption Spectroscopy

Unlike bulk measurements such as radiocarbon and $\delta^{13}C$, sulfur XANES offers a molecular-level view of organic matter redox state and electronic structure. By fingerprinting different S oxidation states present in a sample, XANES provides insight into the origin and diagenetic history of OC (Jalilehvand, 2005; Manceau & Nagy, 2012; Pickering et al., 2001; Poulin et al., 2017; Schroth et al., 2007; Zhu et al., 2016). Here, we used XANES to characterize the compositional heterogeneity of OC within individual samples as well as compare the distributions of organosulfur species between suspended sediment and sediment deposits.

Sulfur K-edge XANES measurements were performed at beamline 14-3 of the Stanford Synchrotron Radiation Lightsource (SSRL) at the SLAC National Accelerator Laboratory. The incident beam was calibrated to have the first pre-edge feature of sodium thiosulfate at 2,472.02 eV. Filter subsamples and aliquots of ground deposit samples were attached to plastic and metal sample trays and measured in a He atmosphere. In most cases, a relatively large section of each sample was mapped initially with 20–25 μm resolution either at the sulfur K-edge (2,482.5 eV) or above the edge (2,510.0 eV) to identify a sulfur-rich region. Subsequently, this subregion was mapped at 5 μm resolution with multiple incident energies characteristic of pre-edge, K-edge, and post-edge sulfur spectral features. A principal component analysis was used to identify map locations of maximum spectral diversity within the high-resolution scan area, which were then selected for collection of complete X-ray absorption spectra. Because this methodology maximizes the sampled diversity of S speciation at the expense of randomly surveying the sample's spectral characteristics, our collection of spectra cannot be viewed as a purely random sampling. One to four replicate spectra were collected depending on signal strength, but often in duplicate, and replicate spectra were averaged together.

Averaged spectra were baseline corrected visually using the SIXPACK software. Spectra with very high pre-edge variability relative to the maximum fluorescent signal, indicative of extremely low S contents, were removed from the analysis (16/138 spectra). Acceptable measurements (122/138 spectra) were subsequently fit to transmission spectra from the European Synchrotron Radiation Facility for sulfate (anhydrite), sulfonate (taurine), sulfoxide (methionine sulfoxide), thiol (cysteine), and disulfide (glutathione disulfide). Fitting was performed through a least squares optimization of proportional error with an inclusion threshold of at least 10% normalized florescence and with all fractional contributions constrained to be positive. The sum of fractional contributions from reference spectra was not required to sum to unity, and reported fitting fractions reflect normalization to the total fit. The same fitting routing was applied at a pixel-by-pixel level on maps collected at multiple incident energies but using all positive florescence responses rather than 10% thresholding. Additional methodological information about our XANES measurements, including an assessment of blank contamination, is included in Supplementary Text 2.

2.4. Topographic and Land Cover Data

During sample collection, we conducted elevation surveys along two valley-perpendicular cross sections using a laser range finder and a handheld GPS unit (TP-XS and FF-XS; Figure 1). We additionally surveyed four cross sections of the river channel near where it enters Lake Haukadalsvatn (Figure 4c). At these and other collection sites, we determined the grain size of the river bed material by conducting a Wolman pebble count. Aerial photography of select portions of the valley was collected using a DJI Phantom quadcopter that was flown manually and programmed to take photographs throughout the flight.

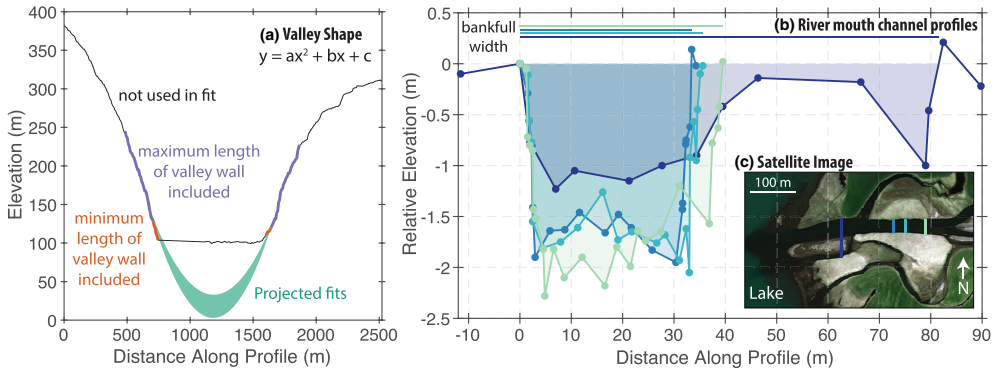

Figure 4. Topographic cross sections. (a) Example cross section taken from the lower valley (Figure 3a). Note the vertical exaggeration. The thin black line shows the raw topographic data from the PRC DEM. The orange colored line indicates the minimum portion of the valley walls that was used to fit a quadratic function for estimating the depth to bedrock (green curves). The combined length of the blue and orange lines indicates the maximum portion used in the fit. (b) Field measured cross sections of the mainstem channel near to the river mouth. The colored lines at the top of the figure indicate the estimates of bankfull channel width from each cross section. (c) Satellite image showing the locations of the cross sections in panel (b).

The field surveys were complimented with a 10 m resolution digital elevation model (DEM) of our study region provided by the National Land Survey of Iceland (NLS; available at www.lmi.is) as well as a 2 m DEM from the Polar Research Center (PRC Porter et al., 2018). The portion of the 10 m NLS DEM that covers our study area appears to have been constructed from a 20 m elevation contour map leading to artifacts in the distribution of elevations within the catchment. While the 2 m PRC DEM lacks such artifacts, it contains some gaps within our study region that complicate the use of flow routing algorithms. Depending on the task, we used either the NLS DEM (flow routing) or the PRC DEM (valley width and depth determination) and show a composite of both in Figure 1. Bathymetric data for Lake Haukadalsvatn were taken from the Reykjavik Energy Authority. Terrain analysis was performed using a combination of GRASS GIS (Neteler et al., 2012) and MATLAB.

To estimate the areal extent of sediment fill in the river catchment (as in Blöthe & Korup, 2013; Mey et al., 2015), we analyzed 200 evenly spaced valley cross sections. For this analysis, we split the valley into an upper and lower portion based on the dominant orientation of the valley axis and analyzed an equal number of cross sections in each region. The location and orientation of the cross sections are indicated by the gray boxes in Figure 3a. Based on field observations and a visual analysis of satellite imagery, the other major tributaries (e.g., Tributary 3; Figure 3) were deemed to not be storing significant amounts of sediment and thus excluded from this analysis.

For each cross section, we applied a moving average smoothing of the raw elevation data and then fit the smoothed data using a smoothing spline. We found the maximum point of curvature closest to the channel to approximate the transition from steep bedrock slopes to the shallow alluviated valley in manner consistent with field observations and aerial photographs. Additionally, we narrowed our search by masking data much higher than the minimum elevation in the profile. Using a Monte-Carlo approach, we randomly varied the smoothing window from 1 to 25 points and the masking elevation from 8 to 12 m above the lowest elevation in the profile and repeated the calculation 100 times. From the Monte-Carlo simulations, we took the maximum estimates of valley width for each cross section, which minimizes abrupt changes in valley width between adjacent cross sections.

To estimate the average depth of valley sediment deposits presently accessible by lateral channel migration (i.e., the thickness of sediment above the river channel bottom at any given cross section), we again used the PRC DEM and analyzed the same set of cross sections. In each cross section, we isolated the region previously defined as the alluviated valley and calculated the difference between each elevation measurement and the minimum elevation within the cross section. For each cross section, we computed the average of the elevation differences and used this a measure of the thickness of sediment that could potentially be entrained by lateral channel migration.

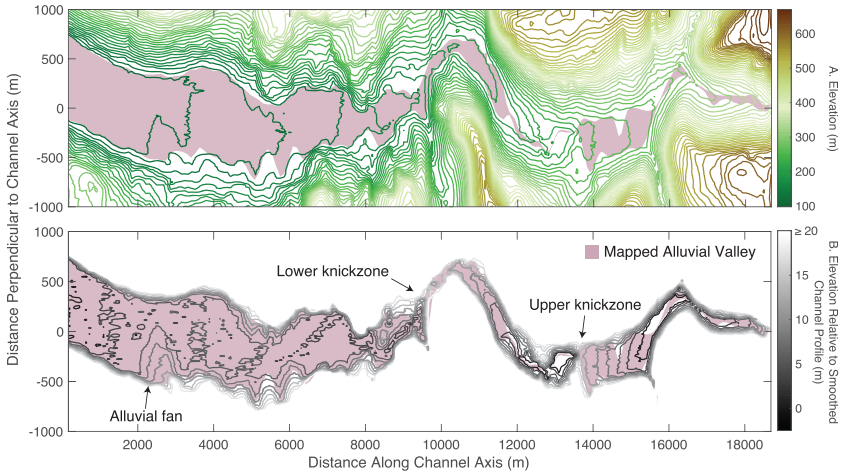

Figure 5. Map of alluviated area. (a) Contour map of catchment elevations re-projected to be along the main channel axes (Figure 3a). The pink area represents the mapped area of alluvial cover. (b) Catchment elevations relative to the river channel profile.

To evaluate the total thickness of valley fill in the lower valley reach, we isolated portions of the bedrock valley walls in each cross section, fit them with a quadratic function, and projected the fit beneath the alluvial cover to find the depth to bedrock in each profile (Figure 4a). A quadratic function was used to describe the shape of the bedrock valley following previous work on glacial systems (James, 1996; Otto et al., 2009). For each fit, we excluded the upper portions of the bedrock walls as they transition to being convex in shape (see Figure 4a). The range of estimates for depth to bedrock using variable valley wall lengths was taken as an estimate of the uncertainty of this approach (Figure 4a). An example cross section is shown in Figure 4a.

Our measurements of alluviated area were combined with both depth measurements to evaluate the total volume of valley fill as well as the volume that is currently above the local river channel bottom. These and subsequent volumetric estimates represent total volumes (sediment volume plus pore volume) and not just the volume of sediment particles as we lack direct measurements of porosity and its variability between deposit types. Since there is internal consistency in our volumetric estimates, including pore volumes does not affect our calculations provided that differences in porosity between sediment reservoirs (e.g., the valley fill vs. the lake deposits) are small relative to differences in total volumes. Instances where differences in porosity have the potential to affect our calculations are evaluated in section 4.3. Our volumetric estimates also do not partition the total volumes between grain size classes.

To display the boundaries of our mapped alluvial area, we re-projected the data to be relative to the direction of the valley axis. In other words, we rotated the gray rectangles in Figure 3a to be even with the X and Y axes (Figure 5). To visualize subtle (<20 m) variations in the topography of the valley floor, we subtracted the elevation of the thalweg of the local river bed (i.e., a single power law fit to the profile in Figure 3b) from each pixel.

For comparison to the automated approach, we manually mapped the area of the valley floor using a combination of the 2 m PRC DEM, a derived slope map, and an orthorectified satellite image (DigitalGlobe GeoEye). With the manual mapping approach, we were able to distinguish glacial deposits (e.g., drumlins and moraines) and evaluate their relative contribution to the alluviated area. Finally, we compared the field measured cross sections to those extracted from the PRC DEM. The consistency between relative elevation changes and cross-sectional area suggests that the PRC DEM has sufficient accuracy and resolution to characterize the fine-scale variability of Efri Haukadalsá valley (Figure S3).

3. Results

3.1. Valley Morphology and River Dynamics

The Efri Haukadalsá River is gravel bedded for most of its length with exceptions of near Lake Haukadalsvatn, where it transitions to being sand bedded, and in some upstream reaches where bedrock is exposed in the channel. These upstream reaches of bedrock exposure in the channel correspond with abrupt increases

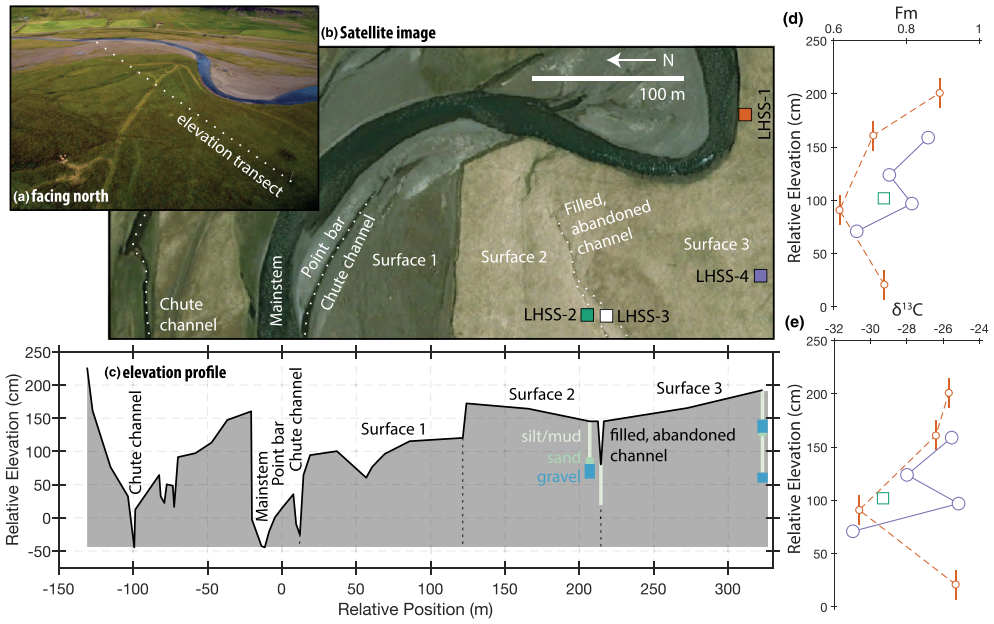

Figure 6. (a) Aerial image showing the location of the lower valley cross section (TP-XS). (b) Annotated satellite image showing fluvial features and sampling locations along the cross section. (c) Field measured elevation profile along with stratigraphic sections showing dominant grain size variations with depth. (d) Depth profile of *Fm* values for POC in adjacent deposits LHSS-1 through LHSS-4. (e) Depth profile of $\delta^{13}C$ values for POC in adjacent deposits LHSS-1 through LHSS-4. Uncertainty bounds on the depth measurements for LHSS-1 account for the fact that this site was not manually surveyed and tied to the other sites.

in channel slope, or knickzones, evident in the long profile (Figure 3b). In the field, waterfalls are observed at both knickzones. The lower knickzone roughly corresponds with our boundary between the upper and lower valleys (Figure 3). At its mouth, three surveys of the channel before it bifurcates constrain the bankfull width and maximum depth of the river to be 36 and 2 m, respectively (Figures 4b and 4c).

The alluviated portion of the valley occupies 7.98 km^2 (~5% of the catchment area; Figure 5a) as estimated using our automated approach. We find that, by area, the valley fill is dominantly contained within the lower valley (84%; Figure 5a). Our visual estimate of valley area (11 km^2) is slightly higher than the estimate from the automated approach but, overall, is close in magnitude. Largely, the automated approach did not include areas occupied by glacial sediments (drumlins and moraines; Figure 1), which we visually mapped to occupy ~3.0 km^2, helping to reconcile the different approaches. Our map of valley elevation relative to the local channel reveals a substantial input of sediment from the southern tributary as shown by an alluvial fan on the valley floor (Figure 5b).

Using the mean thickness of the valley fill, we estimated that a sediment volume of up to 28×10^6 m^3 is currently above the local river channel bottom and thus accessible to the river channel by lateral migration. A majority of this near-surface fill (87%) is located in the lower valley (Figure 5). Using our prediction of bedrock topography beneath the alluvial valley (Figures 3b and 5a), we estimated a total volume of fluvial deposits of up to 147×10^6 m^3 for the lower valley. The total sediment fill in the lower valley is wedge shaped and thickens from the lower knickzone to the lake (Figure 3b). Our most downstream estimates of bedrock topography predict an elevation that agrees closely with the known depth to bedrock beneath the lake from sediment coring (Figure 3b Geirsdóttir et al., 2009).

3.2. Deposit Descriptions

The sediment deposits from both cut banks and floodplain cores are grouped into three types: gravel, sand, and mud (i.e., silt and clay). The gravel is clast supported, imbricated with a matrix of sand/silt (Figures 2b–2d), and of similar size/shape to the gravel on the modern channel bed. As a result, we interpret the gravel deposits as river channel deposits possibly due to lateral channel accretion during meandering. The fine-grained matrix of the channel deposits suggests that they contribute to total POC storage. The sand and mud deposits can be laminated and can contain centimeter-scale lenses of coarse sand and

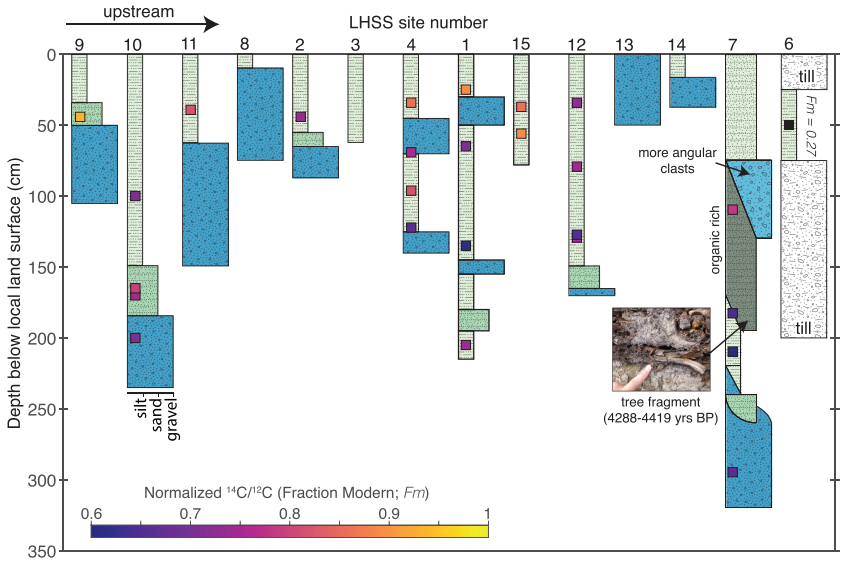

Figure 7. Stratigraphic columns. The colored squares demarcate the locations of radiocarbon samples and the measured values (color scale).

fine gravel (Figure 2b). Iron oxide stained root traces are common and create a mottled texture (Figure 2c). We interpret the sand and mud deposits as deriving predominantly from overbank deposition. For example, we observe that mud fills abandoned channels (Figure 6c). In one location (LHSS-7), a decimeter-scale organic-rich layer (35.4 wt% C) about a meter below the floodplain surface contained numerous tree fragments (Figures 2d and 7). As mentioned in section 2.1, the valley is not presently forested but, in descriptions written by early inhabitants, is described as being forested at the time of settlement (about 874 AD; Geirsdóttir et al., 2009; Grönvold et al., 1995). In Figure 7, we display stratigraphic sections measured at 14 locations across the floodplain.

The upper portions of the catchment contain several glacial deposits including a moraine and drumlins (Figure 1). Some of these features are currently being eroded and entrained by the river channel, indicating that they may contribute to the catchment sediment budget. The texture of the glacial till in these deposits (Figure S4) is distinct from the downstream fluvial deposits (Figures 2b–2d) in their ratio of fine matrix to coarse clasts (the matrix content is greater in the till), clast angularity (the fluvial clasts are more rounded), and sorting (the till deposits appear massive and poorly sorted whereas the fluvial deposits are laminated). In one section (LHSS-7), we observed a vertical change in clast angularity (Figures 2d and 7). We did not visit the headwaters of Tributary 1 and, as a result, did not field check our identification of glacial deposits as was done for Tributary 5 (tributary numbering provided in Figure 3).

3.3. OC Geochemistry

Measured C concentrations range from 0.4 to 35.4 wt% C for deposit samples with a median of 1.2 wt%. This nearly 2 orders of magnitude range in wt% C is consistent with other floodplain studies (Sutfin & Wohl, 2017). Of our 26 samples, only three have concentrations of greater than 4 wt%, and these samples were all collected from the same site (LHSS-7). The most concentrated of these outliers, which was collected from LHSS-7 at 137 cm above the local river bed, resembled peat and contained wood fragments (Figures 2d and 7). The two samples where it was possible to measure suspended sediment concentrations yielded C concentrations of 10 and 19 wt% C.

The $\delta^{13}C$ of deposit samples ranged from −31‰ to −25‰ (Figures 8a and 8b). The variability in $\delta^{13}C$ with depth within an individual deposit was similar magnitude to the variation between deposits (Figure 6e). Depth-dependent variations were not monotonic and have different shapes for each deposit (Figure 6e). Our values agreed with $\delta^{13}C$ measurements of Lake Haukadalsvatn sediments reported by Geirsdóttir et al. (2009), which range from −29‰ to −25‰.

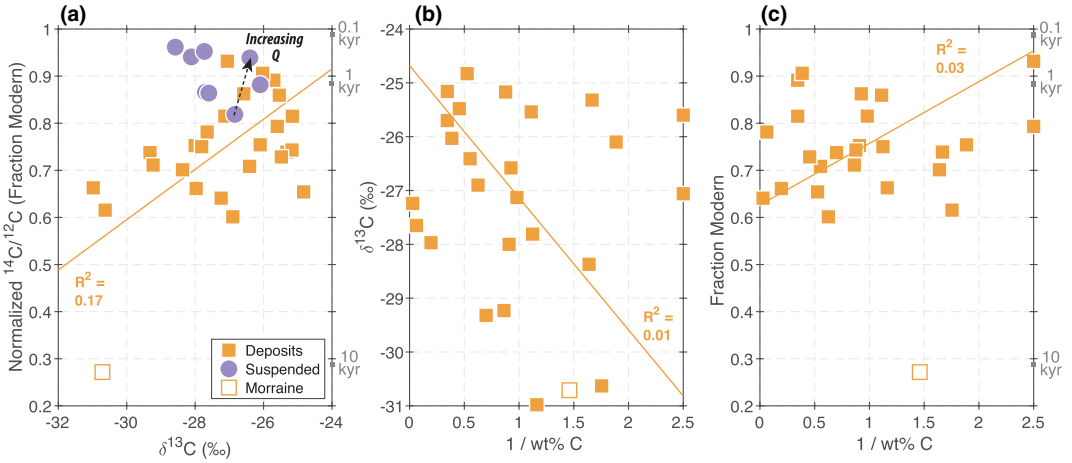

Figure 8. Measurements of radiocarbon and stable C isotopic ratios of POC in suspended sediment (purple circles) and fluvial deposits (filled orange squares). In all cases, the reported $\delta^{13}C$ values were determined after sample acidification on the exact same gas that was used for radiocarbon measurements. A sample of a glacial moraine (open orange square) is also shown for comparison. In panel (a), the black dashed arrow links the two suspended sediment samples collected from the same site under different discharge (Q) conditions. The tip of the arrow points to the sample collected at higher discharge. Due to the lack of concentration measurements for the suspended sediments, these data are not included in panels (b) and (c), which compare the isotopic ratios to the inverse of C concentrations. In all panels, the best fit linear regression for the fluvial deposits is shown along with the R^2 value, which is the expected relationship if the data represented two-component mixing.

Relative to the deposit samples, suspended sediments showed a slightly narrower range of $\delta^{13}C$: −29‰ to −26‰ (Figure 8a). For the single site (LHWS-1) where the $\delta^{13}C$ of suspended sediments was measured at two different discharge (Q) conditions, there was little variation observed (+0.4‰ with increasing Q; Figure 8a).

For deposit samples, the normalized ^{14}C to ^{12}C ratio, or Fraction Modern (*Fm*), ranged from 0.27 to 0.93 (Figures 8a and 8c). The lowest measured value was from a glacial moraine (LHSS-6; Figure 7). Similar to $\delta^{13}C$, depth-dependent variations in *Fm* were not monotonic within a single deposit (Figures 6d and 7). However, horizons within the top ~50 cm of the local land surface displayed, on average, higher *Fm* values than deeper deposits (Figure 7). Distance from the active channel was not a strong predictor of *Fm* at our site (Figure 6), which is consistent with cutoff events changing the position of the channel and direction of migration (Bradley & Tucker, 2013). A single fragment of a birch tree branch found within deposit LHSS-7 at a depth of 1.9 m below the local land surface (Figure 7) yielded a calibrated radiocarbon age estimate of 4,288 to 4,419 years before present (95% confidence interval using MatCal; Lougheed & Obrochta, 2016).

Relative to the deposits, the suspended sediment samples showed higher *Fm* values that range from 0.81 to 0.96 (Figure 8). A two-sample Kolmogorov-Smirnov (K-S) test yields a p value of 3×10^{-4} for the *null* hypothesis that the *Fm* values of the suspended sediments and the fluvial deposits (i.e., not including the moraine) were potentially drawn from the same distribution.

Two-component mixing predicts a strong linear covariation between either $\delta^{13}C$ or *Fm* and the inverse of C concentrations. To test for two-component mixing, we fitted linear models to our deposit data (not including the moraine sample) using reduced major axis regression (Figure 8). Overall low R^2 values (0.17, 0.01, and 0.03 for $\delta^{13}C$ vs. *Fm*, 1/C vs. $\delta^{13}C$, and 1/C vs. *Fm*, respectively) imply that the variability in our data set cannot be explained by two-component mixing alone. Instead, our data require more OC sources, variable aging, and/or stable isotopic fractionations.

3.4. Organic Sulfur Geochemistry

Measured XANES spectra show S compounds of mixed-oxidation state in both fluvial deposits and suspended sediments (Figure 9a). The spectra indicate the presence of both reduced S moieties such as thiol and sulfoxide, as well as oxidized moieties such as sulfonate and sulfate. This significant heterogeneity in redox state occurs at all scales, from an individual spectra to individual samples, as well as across samples from different locations in the catchment (Figure 9b).

To quantify the relative proportions of different S redox states, we fit each spectra to the sum of five reference materials (Figure 9c). These fittings results are summarized using the statistic F_{red}, which is the sum

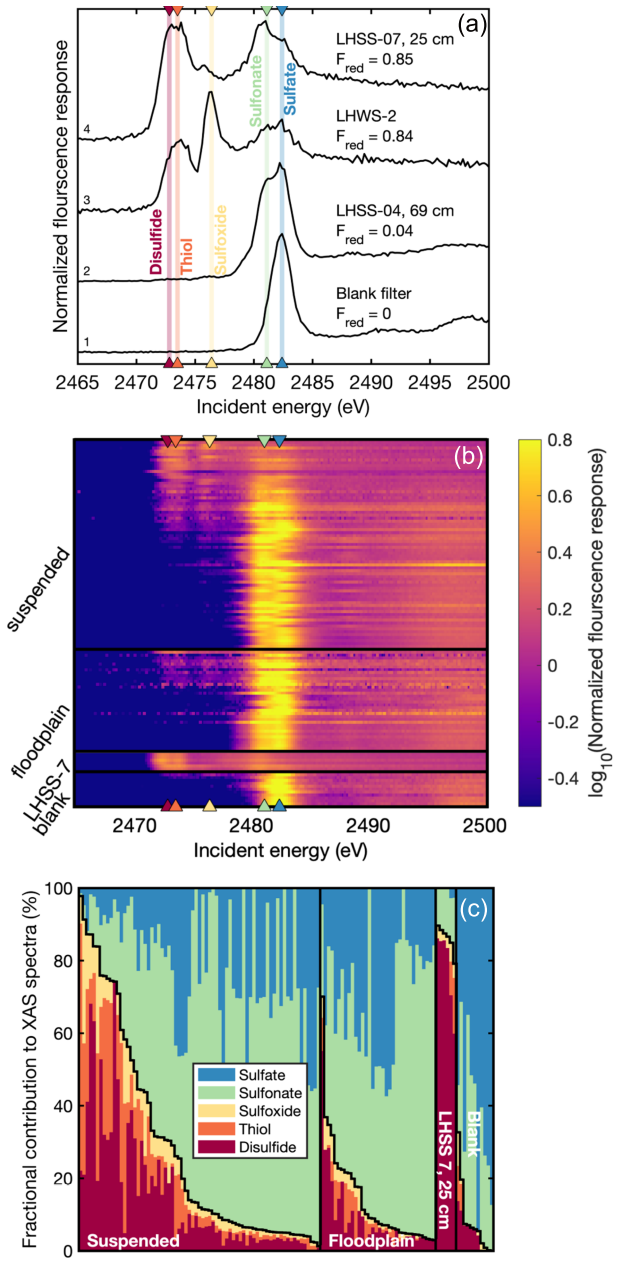

Figure 9. (a) Four example spectra including fluvial deposits, suspended sediment, and a blank filter. Vertical shading with triangular end points indicate the characteristic response locations of disulfide, thiol, sulfoxide, sulfonate, and sulfate. The sum of the normalized fractional contribution of the three most reduced phases (F_{red}) is indicated. (b) Waterfall plot of XAS spectra taken on suspended sediments, fluvial deposits, and blank filters. LHSS-7 at 25 cm has a major peak at low incident energy, distinct from other fluvial deposits, and is plotted separately. (c) Fractional contributions of reference materials to measured spectra. Suspended sediments and fluvial deposits both contain a variety of redox phases.

of the fractional contributions from disulfide, thiol, and sulfoxide and reflects the abundance of reduced sulfur moieties relative to total sulfur present. The collected absorption spectra showed a wide range of values of F_{red}, indicating a range of sulfur valence states in both suspended sediment and floodplain/valley fill deposits. For reduced moieties, the fitting found a significant but variable contribution from organic disulfides, sulfoxides, and thiols in both suspended sediments and fluvial deposits. For the oxidized moieties, the fitting revealed substantial fractional contributions from both sulfonate and sulfate.

4. Discussion

4.1. Millennial-Scale POC Storage

Our radiocarbon measurements of OC in riverine suspended sediments and fluvial deposits were all significantly older than "modern" (i.e., 1950 CE). Unlike at other field sites (Bouchez et al., 2010; Galy et al., 2008; Masiello & Druffel, 2001), these old ages cannot be attributed to petrogenic OC as there are no sedimentary rocks in the catchment. Apparent radiocarbon ages for OC stored in the fluvial deposits range from 315 to 4,090 years and thus suggest centennial to millennial-scale OC storage. Consistent with this, the calibrated radiocarbon age of 4,288 to 4,419 years before present for a tree branch within a fluvial deposit implies that sediment storage times within the catchment are of sufficient magnitude to explain the bulk OC radiocarbon data. Sediment storage on hillslopes may have also contributed to the bulk *Fm* values; however, based our observations of steep valley walls with thin soils (Figure 2a) and the aforementioned correspondence between deposit ages (tree fragment) and bulk *Fm* values, we interpreted these results in the context of fluvial storage.

The oldest material measured in the catchment was from a glacial moraine (Figure 8). While moraine deposition is a mode of sediment storage and relates to the efficacy of fluvial sediment transport (the moraine is presently being incised by the river), moraine storage reflects a different set of mechanisms than fluvial storage (Bradley & Tucker, 2013; Torres et al., 2017) and might be characterized by a narrower age distribution associated with a time period of relative stability of a glacier ice margin. It is possible that the radiocarbon depletion measured in POC from fluvial deposits downstream of the moraine is, in part, due to the incorporation of POC sourced from moraine erosion. However, stable carbon isotopes and their covariation with radiocarbon suggest that glacial OC is not the sole source of aged carbon in the catchment (Figure 8). Specifically, the low concentration of C in the moraine and its low $\delta^{13}C$ value cannot account for the extent of radiocarbon depletion in samples with higher $\delta^{13}C$ values and C concentrations (Figure 8). To further evaluate the role of glacial OC inputs, we collected multiple XANES spectra on a sample from the moraine (LHSS-06). These spectra indicate the presence of S species that are predominantly oxidized (+5 and +6 valence), and, given the presence of reduced S moieties in our other samples, we disfavored the hypothesis that the aged carbon in this catchment derived solely from the moraine (Figure 9). We revisit the potential contributions of moraine OC to total OC storage in the Efri Haukadalsá catchment in sections 4.2.2 and 4.4.

4.2. Heavy-Tailed Storage Impacts on Biogeochemistry

4.2.1. Evidence From OC

Our measurements of suspended sediment spanned a narrower range of *Fm* values, are shifted toward higher *Fm* values overall, and likely represent a different age distribution (based on a K-S test; section 3.3)

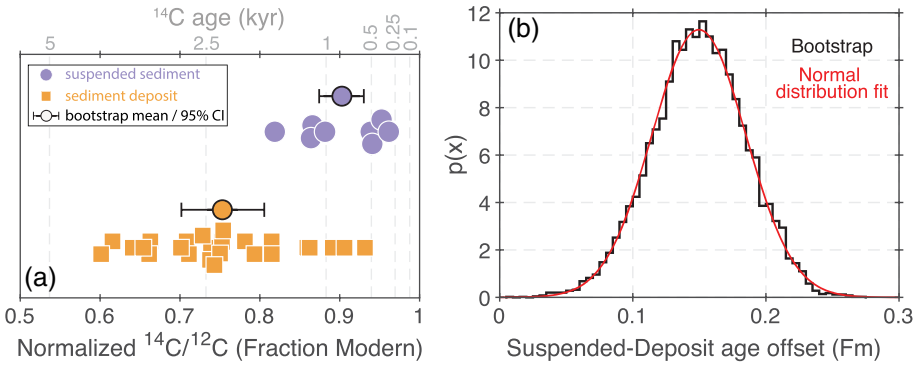

Figure 10. (a) Distributions of *Fm* values for suspended sediments (purple circles) and sediment deposits (orange squares) along with means for each group calculated via a bootstrap resampling procedure. (b) Age offset between suspended sediments and sediment deposits calculated using the bootstrapped mean values.

relative to the deposits (Figure 10). Due to active channel migration, it is likely that the cut banks, at any given time, entrain deposits of all different origins—including coarse-grained lateral accretion sets, fine-grained overbank deposits, and abandoned channel fills. While our deposit samples reflect only a small sampling of the likely wide distribution of deposit ages and facies on the floodplain, the suspended sediment samples are likely integrating across a range of these deposits. In this way, the suspended sediments provide a measure of the OC that is actively being exported from the system and are complementary to the deposit samples. The observed pattern in the deposit and suspended sediment *Fm* values suggests that "young" OC is preferentially exported from the catchment relative to "old" OC, which is favored in the fluvial deposits. Likely, this is due to how the river samples its floodplain reservoir (Bradley & Tucker, 2013; Torres et al., 2017). So we interpreted the difference in *Fm* as evidence that age-biased sediment storage and transport impacts the age distribution of terrestrial POC (consistent with the predictions of Torres et al., 2017). This interpretation assumes that our samples are representative of the catchment system in both space and time, which we discuss further below.

Our individual data points represent small masses of OC relative to the total mass of OC stored in the catchment or exported annually. As such, it is difficult to directly constrain the average *Fm* of either OC pool as we lack the necessary information to weigh each data point by its OC concentration, deposit volume, and bulk density. So, instead, we took a boot-strapping approach and resample our data with replacement to calculate average *Fm* values along with the mean age offset between the suspended sediment and deposit samples (Figure 10). The details of this calculation are provided in the supporting information MATLAB script. Briefly, we resampled each data set eight times (i.e., the total number of suspended sediment measurements) with replacement, computed an average, differenced the averages, and repeated for a total of 10^4 trials. The result of this calculation yielded a mean age offset of 0.15 ± 0.04 (1σ) *Fm* units (Figure 10). In radiocarbon years, this offset is equivalent to the deposits being on average 1.4 kyr older than the suspended sediments.

In addition to the boot-strapping approach, various features of the data set support a significant age offset between the suspended sediment and deposit samples. For example, sampling at station LHSS-1 before and during a storm event revealed that, at higher stage, the *Fm* of the suspended sediments shifted to higher values (0.82 to 0.94; Figure 8). Since rivers tend to export more POC at high stage (Hilton, 2017; Turowski et al., 2016), the higher *Fm* values might be considered more representative of the mean age of exported POC—integrated on time. If correct, this furthers the discordance between age of the suspended sediment and that of the deposits. Additionally, we observed that the fluvial deposit samples with the highest *Fm* values tended to be limited to the top ~50 cm of each deposit and thus, as a fraction of total deposit depth, made up a smaller proportion of the total fluvial deposit OC reservoir (Figure 7). Thus, the slight overlap in the range of *Fm* values for the suspended sediment and deposit samples (Figure 10) represented samples that were less likely to represent the average *Fm* value for either OC pool.

The suspended sediment samples were not collected during bankfull flow conditions and, as a result, may not reflect the average composition of exported OC (Hilton, 2017; Turowski et al., 2016). Based on single storm sample (sub-bankfull flow), we predict that our suspended sediment samples are biased old (see

above; Figure 8a), but we lack a complete data set to fully constrain the relationship between river discharge and *Fm*. The OC preserved in the sediments of Lake Haukadalsvatn, which contains an integrated record of riverine OC export, showed a range of bulk $\delta^{13}C$ values (−29‰ to −25‰) that matched our suspended sediments samples (−29‰ to −26‰). In contrast, the fluvial deposits showed a wider range of $\delta^{13}C$ values that exceeds what was observed in the lake sediments (Figure 8Geirsdóttir et al., 2009). So, at least in terms of stable isotopic compositions, our suspended sediment samples matched the average composition of exported OC.

The lake sediment data set of Geirsdóttir et al. (2009) also includes ^{14}C measurements. However, they only measured base-extractable OC ("humic acid") for its radiocarbon content, which routinely has a significantly different *Fm* than bulk OC (Abbott & Stafford, 1996; Martin & Johnson, 1995) and/or macrofossils (Brock et al., 2010; McGeehin et al., 2001; Wolfe et al., 2004) at the same stratigraphic horizon and can show significant intrasample age heterogeneity (Brock et al., 2010; McGeehin et al., 2001). Presumably, the differences in *Fm* result from differences in the cycling rates of humic acids versus bulk OC and that fact that neither of these OC pools have a defined composition and instead refer to a heterogeneous mixture of various molecules. Importantly, the known differences in *Fm* between bulk OC and humic acids imply that the ^{14}C measurements from Geirsdóttir et al. (2009) are not directly comparable to our data. Nevertheless, we calculate the decay-corrected *Fm* values of the most recent base-extractable OC from Geirsdóttir et al. (2009) to be 0.80 and 0.81 (155 and 164 cm depth). These *Fm* values are stratigraphically reversed (i.e., the older "age" is shallower in the core). Both of the *Fm* values from the lake sediment core are in between our bootstrap estimates of mean fluvial deposit and mean suspended sediment *Fm* values (Figure 10). While these data are difficult to compare for methodological reasons, it also worth noting that our suspended sediment and fluvial deposit samples likely incorporate some proportion of C fixed during atmospheric weapons testing, which postdates the deposition of the samples measured by Geirsdóttir et al. (2009). This would have the effect of increasing the *Fm* values of our samples relative to those of Geirsdóttir et al. (2009) without requiring a change in storage dynamics. So, while there is a slight overlap between the present day fluvial deposits and the decay-corrected lake sediment *Fm* values, this is not inconsistent with our interpretation of age-biased OC export given known differences between bulk and humic acid *Fm* values and anthropogenic increases in atmospheric ^{14}C.

Strictly, our data set supports an *instantaneous* age offset between exported POC and POC stored within the catchment (Figure 10). However, based on the preliminary age-discharge relationship (Figure 8) and the close match between the $\delta^{13}C$ of bulk lake sediments (Geirsdóttir et al., 2009) and riverine suspended sediments (Figure 8), we hypothesize that this age offset might be a general feature of the catchment. In order for the river to export OC in an un-age-biased way, the river channel would have to randomly and uniformly sample the fluvial deposit reservoir, which is inconsistent with the known physical dynamics of lateral channel migration (Bradley & Tucker, 2013; Torres et al., 2017) and observations of chute cutoffs focused around the modern river channel in the study catchment (Figure 2a).

Lastly, our topographic analyses revealed a large quantity of sediment stored beneath the channel that is presently shielded from entrainment within a glacial overdeepened valley (Figure 3b). While this reservoir may include some gravel deposits, we found that the fine matrix within surface exposures of coarse-grained deposits contained appreciable concentrations of POC with a low *Fm* (Figure 7). Alternatively, some of the deep sediment may be past fine-grained bottomset (lacustrine) deposits reflecting long-term delta progradation. In either case, the deep valley fill is a reservoir of OC that should be aged relative to the pool of OC presently accessible by lateral channel migration due to its stratigraphic position. Thus, despite omnipresent uncertainties in just how representative our samples are for this system, the independent evidence for long-term sediment aggradation (Figure 3b) implies substantial storage of OC that is older than the OC that is currently being exported from the system.

4.2.2. Evidence From Organic Sulfur

In addition to bearing the fingerprint of age-biased export (Figure 10), our radiocarbon measurements may also reflect additional processes. For example, we observe that an ancient moraine preserves aged OC and supplies sediment to the catchment (Figure 8). Inheritance of pre-aged OC can decrease *Fm* measurements and influence how the *Fm* of a deposit evolves in time during storage. However, inheritance alone cannot produce an age offset as pre-aged OC is contributed to both fluvial deposits and suspended sediments. Instead, the magnitude of the age offset can be affected by the continued production and consumption of

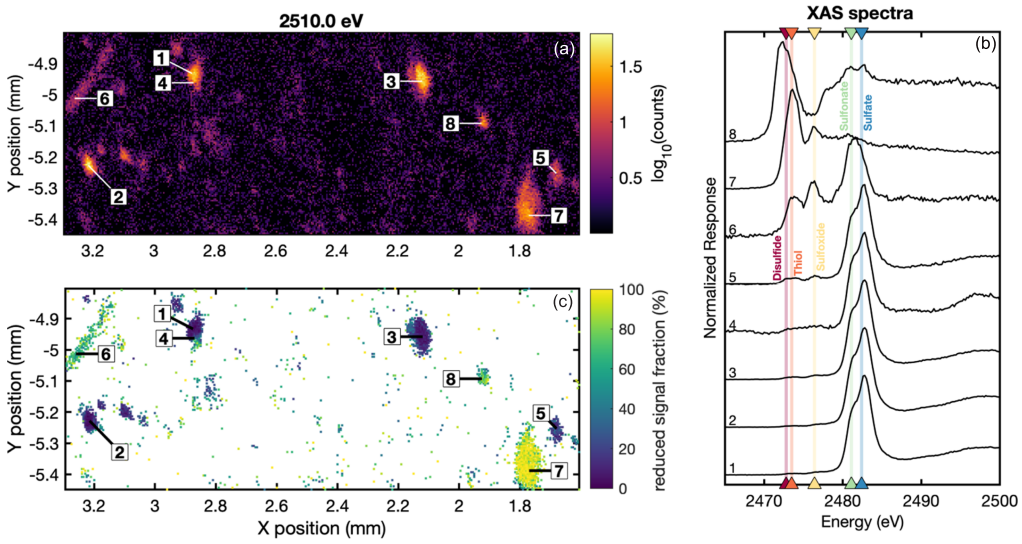

Figure 11. (a) Fluorescent response at an incident energy of 2,510.0 eV for sample LHWS-13. Because all oxidation states of S are expected to fluorescence similarly at this incident energy, the colorscale represents the abundance of S. Numbered points indicated locations of collected XAS spectra. (b) Normalized XAS spectra show both reduced and oxidized phases. Vertical shading with triangular end points indicate the characteristic response locations of disulfide, thiol, sulfoxide, sulfonate, and sulfate. (c) Pixel-by-pixel fitting of the fluorescent response at multiple incident energies identifies coherent groupings, which are interpreted as particles with distinct redox characteristics. Pixels are shown only where there is a significant fluorescent response at an incident energy of 2510.0 eV.

OC during storage (Torres et al., 2017). For example, if the "old" OC stored in the fluvial deposits is replaced with "young" OC, their bulk *Fm* will be shifted toward the values measured in suspended sediments.

The presence of a variety of S oxidation states in our POC samples is consistent with OC cycling during storage (Figure 11). In many suspended sediment samples we observed multiple particles in close association that diverge strongly in their S redox states. For example, spectra on the suspended sediment sample LHWS-13 identified five regions of mostly oxidized S and three regions where S is strongly reduced (Figure 11). This diversity of spectral characteristics is inconsistent with a single source and history but rather is consistent with differential storage, processing, and remobilization of OC. The same diversity of redox states was found in XAS spectra collected from POC in fluvial deposits (Figure 9), although the imaging was less meaningful due to sample homogenization prior to analysis.

To further evaluate the relative roles of catchment history, fluvial morphodynamics, and OC cycling in setting age structure of OC stored in the Efri Haukadalsá catchment, we adopted the forward modeling approach of Torres et al. (2017). The sediment storage component of this model could be calibrated for our catchment using constraints of storage volumes and exchange fluxes derived from remote sensing and field measurements (section 4.3).

4.3. Spatiotemporal Scales of Sediment Transport and Storage

Sediment transit times through river floodplains are predicted to follow a tempered Pareto distribution (Bradley & Tucker, 2013; Torres et al., 2017) ast a consequence of channel migration approximating a boundedt random walk process. Torres et al. (2017) provide a dimensionless tempered Pareto distribution derived fromt meandering model simulations (Howard & Knutson, 1984; Limaye & Lamb, 2013) that can be rescaled fort application to natural systems using two parameters: a characteristic transport length scale (x_{tran}) andt a characteristic channel migration timescale (T_{cut}). These model parameters can be constrained using a sedimentt budget and observations of channel migration. The overall slow rates and small size of the channelt (width ≈ Landsat resolution) made it challenging to determine lateral migration rates for the Efri Haukadalsá Rivert using a time series of Landsat images (e.g., following Schwenk et al., 2017). However, workt by Constantine et al. (2014) and expanded on by Torres et al. (2017) suggested that migration rates are correlated witht sediment fluxes for many rivers. As a result, it was possible to generate an approximate calibrationt for the Torres et al. (2017) model from the sediment budget alone.

In essence, thet tempered Pareto distribution provided by the Torres et al. (2017) model predicts the amount of time it takes the channel to return to a previous position, which, for a single storage event and in the

absence of aggradation, is the deposit age. In aggrading systems, the Torres et al. (2017) model can still be applied if the rates of vertical sediment accumulation are known and assumed to be spatially uniform. In this case, the age of a deposit evolves in time following the prescribed aggradation rate until the channel returns to this previous position after a period of time dictated by the tempered Pareto distribution.

4.3.1. Estimation of Sediment Fluxes

We estimated the sediment flux (Q_{sed}) for the Efri Haukadalsá River using the volume of sediment preserved in Lake Haukadalsvatn and the age-depth relationship of these sediments. This approach assumed that a majority of the exported sediments were trapped within the lake; this was supported by the steep bathymetry on the outlet side of the lake (Figure 3b) and the fine grain size of the lake sediment deposits (Geirsdóttir et al., 2009).

Using the dates of 24 depth horizons (14 tephra layers and 10 ^{210}Pb measurements) reported from the Lake Haukadalsvatn sediment core by Geirsdóttir et al. (2009), we calculated an average sedimentation rate of 1.6 ± 0.1 m kyr^{-1} over the last 10 kyr by linear regression. This estimate agreed with the average sedimentation rate reported by Geirsdóttir et al. (2009) despite methodological differences in the age models applied (i.e., linear vs. nonlinear models). Geirsdóttir et al. (2009) estimated sedimentation rates up to 3.0 m kyr^{-1} for just the 20th century interval using ^{210}Pb only. This discrepancy between the recent and long-term rates may reflect the timescale dependence of sedimentation rate measurements (Sadler, 1981). Alternatively, the increase in rate could have arisen due to the progradation of the delta toward the location of the sediment core with time or, at least partly, from sediment compaction. Since our ^{14}C measurements imply millennial-scale storage, we posit that a longer-term average sedimentation rate is more appropriate for our calculations and thus use it for our study.

Using a lake area of 3.3 km^2 (Geirsdóttir et al., 2009) and assuming that sedimentation rates are close to uniform in space, we calculate a volumetric sedimentation rate of $5{,}280 \pm 330$ m^3 yr^{-1} (sediment plus pore volume). Using an upstream catchment area of 170 km^2 and sediment densities ranging from 0.3 (the minimum bulk density for the regional soil type Arnalds, 2004) to 3 g cm^{-3} (pure basalt), our mean Q_{sed} estimate translates into an area-normalized mass flux ranging from 9 to 93 tons km^{-2} yr^{-1}, which is comparable to sediment gauging measurements made elsewhere in Iceland (Gislason et al., 2009).

Our estimate of Q_{sed} derived from the lake sedimentation rate only captures a portion of the total sediment production within the Efri Haukadalsá River catchment. Based on our observation of a decimeter-scale fill of sediment beneath the lower valley (Figure 4) and the known glacial history of the catchment (Geirsdóttir et al., 2009), we expect that the valley above the lake has also been filling with sediment over time. Using our estimate of the total volume of valley sediment fill and the assumption that sediment filling commenced from a bare bedrock valley roughly 10,000 years ago (Geirsdóttir et al., 2009), we estimate an average valley fill growth rate (Q_{vfg}) of ~14,700 m^3 yr^{-1}. Assuming the porosity of the lake sediment and the valley fill are approximately the same, the difference in volumetric rates (5,280 vs. 14,700 m^3 yr^{-1}) indicates that sediment is preferentially (~70%) trapped in upstream portions of the catchment as oppose to accumulating in the lake. Alternatively, if the porosity of the valley fill was roughly twice the porosity of the lake sediment, then the volumes of sediment accumulated per unit time would be nearly equivalent for the lake and upstream valley. This latter case is unlikely as the lake sediments are finer grained than the valley fill deposits (Figure 7; Geirsdóttir et al., 2009) and, for unconsolidated sediments, finer grain sizes tend to form deposits with a higher porosity.

4.3.2. Estimation of the Transport Length Scale and Channel Migration Timescale

Following previous work (Lauer & Parker, 2008; Pizzuto et al., 2017; Torres et al., 2017), a characteristic length scale of sediment transport was defined by balancing the downstream sediment flux (Q_{sed}) with the volumetric rate of bank sediment exchange. Bank exchange is driven by lateral migration, and so the volumetric rate was taken as the product of the mean lateral migration rate (E_L; m yr^{-1}), the channel depth (h), and the reach length considered. Setting Q_{sed} and the volumetric rate of bank sediment exchange equal, the resulting reach length represents the length of channel needed to exchange the entire downstream sediment flux with the floodplain once (x_{tran}). By comparing x_{tran} to the observed length of channel, it is possible to infer whether sediments are likely to enter and exit storage multiple times as they transit the system.

Using a power law fit to the empirical relationship between dimensionless lateral migration rates and width-normalized sediment fluxes (Constantine et al., 2014; Torres et al., 2017), our lake sedimentation rate estimate of Q_{sed}, and our determination of bankfull channel width by field surveying (Figures 3b and 3c),

we estimated E_L for the Efri Haukadalsá River. To handle correlated errors and the constraint that lateral migration rates must be positive, we propagated the uncertainties in the regression and input parameters using a Monte-Carlo approach. This yielded a median estimate of 0.5 m yr^{-1} with a 95% confidence interval of 0.25 to 2.5 m yr^{-1}.

To check this estimate of E_L, we visually compared Landsat images collected in 1987 and 2018, which, despite the resolution limitations, should reveal reaches migrating greater than 1 m yr^{-1} (i.e., movement ≥1 pixel). We found that only a few, rapidly migrating reaches moved at rates ≥1 m yr^{-1} and that, for most of the channel length, no movement was detectable at the resolution afforded by Landsat images.

Using the constraint from Landsat images that E_L is less than 1 m yr^{-1} along with an average channel depth of 2 m (from field surveying; Figure 3b), we determined a median estimate of $x_{tran} = 6$ km with a 95% confidence interval of 3 to 10 km. Following the approach of Torres et al. (2017) and taking the nearest integer ratio of the total channel length (21 km) and x_{tran}, we predicted that sediment enters and exits storage an average of two to seven times during transit through the valley of the Efri Haukadalsá River. Given that the majority of the storage in this system is concentrated within just the lower reach, it is likely that the number of storage events is closer to 1 or 2 given the shorter channel length of the lower valley reach (~13 km). For our calculations, we assumed one transport event as this represents a maximum age offset expected for this system.

To constrain the characteristic channel migration timescale (T_{cut}), we assumed that the maximum rate of lateral channel migration was three times the mean rate and use the model prediction from Torres et al. (2017) that T_{cut} was 13.6 ± 3.3 times the duration required to migrate one channel width at the maximum migration rate. Using the same Monte-Carlo approach as above, we estimated a median T_{cut} of 280 years with a 95% confidence interval of 49 to 642 years.

4.3.3. Estimation of Aggradation and Progradation

We observed that a majority of the valley fill in the Efri Haukadalsá catchment is contained within the lower valley and thus limited our analysis to the evolution of this lower sediment reservoir. The bedrock profile of this lower reach is bounded on the upstream end by a bedrock knickzone and on the downstream by steep bedrock outcrops. This suggests that the downstream bedrock zone controls the lake level, and thus, we assumed that it has been approximately constant since deglaciation.

The above constraints and assumptions support a geometric simplification where the total valley fill is approximated as a wedge of sediment described by a topset slope (S_{top}), a foreset slope (S_{for}), and a bedrock slope (S_{bed}). For our analysis, the slope break between the topset and foreset was held at a fixed elevation based on the assumption of a constant lake level. Starting from bare bedrock, we assumed that the sediment wedge prograded and aggraded with a fixed geometry. In this scenario, mass balance dictates that the progradation rate is equal to the ratio of volumetric sediment supply (Q_{vfg}) and the cross-sectional area of the valley. For a constant rate of sediment supply, both the increase in valley cross-sectional area with elevation and the divergence between S_{top} and S_{bed} lead to a decrease in the progradation rate with time. Since aggradation and progradation occur in a fixed ratio (aggradation rate = progradation rate × S_{top}), aggradation rates should also have slowed with time.

To approximate S_{top}, we used a linear fit to channel long profile for the lower valley reach ($S_{top} = 0.003$). To approximate the cross-sectional area of the valley, we used a representative quadratic fit to the bedrock topography (i.e., Figure 4a). For the estimated modern thickness of sediment (cross-sectional area = ~ 6×10^4 m^2), thegeometric model predicted an aggradation rate of ~0.1 cm yr^{-1}, which, given the general U-shape of the valley, should be reasonably representative for the interval of time over which sediments above the modern river channel accumulated. This rate estimate suggests that the average floodplain relief above the channel bed of 3.8 mv was constructed by aggradation over millennial timescales. Consequently, for regions of the floodplain that have been abandoned for thousands of years, the age structure may have been more affected by aggradation associated with progradation of the river delta into the Lake Haukadalsvatn than it was by lateral migration.

4.4. Comparing OC and Sediment Age Distributions

With the above constraints on lateral channel migration and vertical aggradation, it was possible to calculate an ensemble of age distributions for both the sediment stored on the landscape and the sediment exported

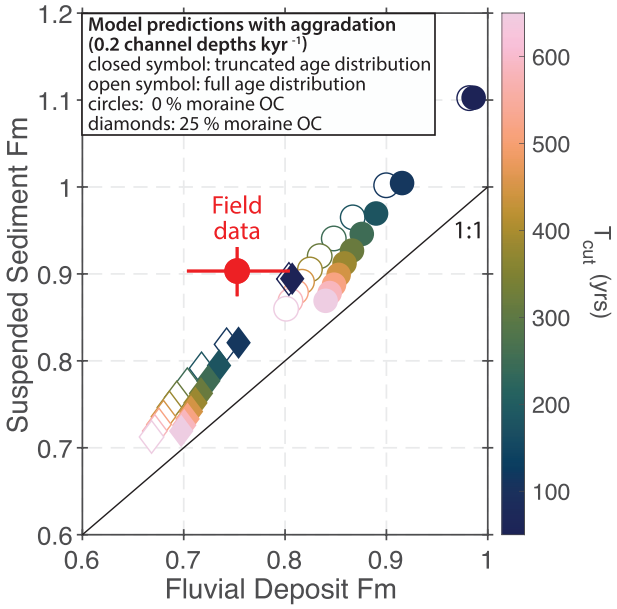

Figure 12. Comparison of sediment and OC age distributions. The colored points indicate model predictions of the mean *Fm* of OC in fluvial deposits (*x* axis) and suspended sediments (*y* axis) assuming that the age distributions follow a model similar to Torres et al. (2017) using different values of T_{cut} consistent with the sediment budget. All points are generated from model simulations that include channel aggradation at a rate of 0.2 channel depths per thousand years. The open symbols show the full age distribution (i.e., including sediments older than deglaciation). The closed symbols show age distributions where sediments older than 13 kyr have been removed. The diamonds indicate simulations where there is an additional pre-aged OC source that represents 25% of the OC budget and is inert during storage (meant to represent OC from the erosion of glacial deposits). Atmospheric variations in $^{14}C/^{12}C$ are accounted for using the calibration curve provided by Lougheed and Obrochta (2016) as well as the assumption that all OC fixed after 1950 has a *Fm* of 1.5 due to the incorporation of ^{14}C released from nuclear weapons testing. The red point with uncertainty bounds shows the bootstrap estimates of the mean *Fm* values for the Efri Haukadalsá River catchment (Figure 10).

by the river. For these estimates, we assumed single values for number of storage events and the aggradation rate (1 storage event and 0.2 channel depths per year, respectively) but varied T_{cut} over its 95% confidence interval. For each simulation, we assumed that all of the model parameters remained constant in time. As such, discrepancies between the model predictions and field data may stem from variations in components of the sediment budget in time that are not considered in the model. However, the near-surface sediments we sampled likely do not record the full evolution of the valley due to sediment burial beneath the channel as a result of valley aggradation. So, while we expect that certain model parameters did evolve in time (e.g., the aggradation rate), the amount of variation during the period of time recorded in our POC samples may be small enough for our assumption of constant parameter values to be reasonable.

Some of the age distributions generated by our model predict that a fraction of the sediment leaving the catchment was stored for longer than 10 kyr. Since the valley is only ~10 kyr old, it is impossible for sediment older than this age to be part of the export flux. This discrepancy reflects the fact that the Torres et al. (2017) model produces a steady-state age distribution, but the Efri Haukadalsá River may be too young to have reached a steady state with respect to sediment age. To account for this, we show both the full model-predicted age distributions (open symbols) and distributions where ages greater than 10 kyr have been removed (closed symbols) in Figure 12. Such a truncation of the age distribution is broadly consistent with model behavior (Bradley & Tucker, 2013).

All of the model-predicted age distributions were transformed into radiocarbon units using the radioactive decay equation and a time series of atmospheric $^{14}C/^{12}C$ for direct comparison to our OC measurements. This transformation effectively assumes that OC has the same age distribution as sediment and that sediment of all ages contributes the same mass of OC. Together, these assumptions represent a useful *null* hypothesis of a scenario with zero OC cycling. The model developed in Torres et al. (2017) does not consider ages less then T_{cut}, does not account for aggradation, does not predict the residence time distribution (i.e., the distribution of deposit ages), and does not account for temporal variations in atmospheric $^{14}C/^{12}C$. Consequently, we provide an updated code as supporting information that includes these additional calculations.

The model predictions with aggradation were able to match the mean *Fm* of suspended sediments but were too young to match the mean *Fm* of the fluvial deposits (Figure 12). Including an additional aged OC source (i.e., glacial sediments) that accounts for 25% of the total OC reservoir allowed the model to more closely fit the data. However, we lack constraints on the proportion of glacial OC within our samples, which along with uncertainties in T_{cut} and the aggradation rate, hindered more detailed model-data comparison. Nevertheless, the degree to which the field measurements are younger than the model predictions constrains the possible magnitude of OC cycling in setting the OC age distribution. Our data do not rule out a greater age offset than predicted by the sediment storage model (Figure 12), which is inconsistent with "simple" OC cycling models where the concentration and isotopic composition of OC change monotonically with time (e.g., Torres et al., 2017) as these dynamics act to decrease the age offset. Potentially, this may indicate recent changes in OC cycling rates and/or nonmonotonic changes in the OC concentrations and/or isotopic compositions with time during storage (see Torn et al., 1997).

As mentioned previously, the vegetation community in the Efri Haukadalsá River catchment is thought to have changed over 300 years ago, which may have affected OC cycling and radiocarbon budgets. Similarly, the bulk POC content of sediments deposited in Lake Haukadalsvatn began to increase 2,000–3,000 years ago (Geirsdóttir et al., 2009), which may also signal important changes in OC cycling in the ecosystem. However,

these changes in vegetation and OC export in and of themselves would not produce an age offset between stored and exported POC without age-biased sediment storage and transport. Instead, they may explain the differences between the "pure" storage model and the field data (Figure 12). Alternatively, the suspended sediments may contain a component of living or recently living "autochthonous" OC that contributes more to the exported sediments as opposed to stored sediments (e.g., aquatic vegetation and incipient vegetation on point bars), though we observed similar distributions of organic S species (Figure 9) and an overlap in $\delta^{13}C$ values (Figure 8) between sediment types that support a compositional similarity between OC in deposits and suspended sediments.

5. Conclusions

Using the Efri Haukadalsá River catchment as a case study where petrogenic OC contributions can be neglected, we observed substantial, millennial-scale OC storage times in terrestrial landscapes. Long OC storage times require a physical reservoir that is stable for at least as long as OC, which in the case of the Efri Haukadalsá, is largely provided by fluvial deposits. Such reservoirs must also be geochemically favorable for OC storage (e.g., low O_2 availability), but this appeared to be the case in the Efri Haukadalsá River catchment based on the ^{14}C data and XANES observations of reduced S species observed in the organic matter present there. Evidence for millennial-scale OC storage is becoming widespread in fluvial systems (Galy & Eglinton, 2011; Lawrence et al., 2015; Tao et al., 2015; Torres et al., 2017), suggesting that the results seen in this study might be generally applicable to a wide range of landscapes. We observed that the timescales of sediment and OC storage, in addition to sequestering CO_2, can also influence OC biogeochemistry by modulating the length of time for chemical reaction to occur influencing OC molecular compositions (e.g., S speciation).

In our study site, we identified two fluvial mechanisms that may allow the landscape to store POC: lateral channel migration and vertical deposit aggradation. The dynamics of lateral channel migration influenced the age distribution of POC exported at any moment by rivers, whereas aggradation created a subsurface reservoir of OC that can be sequestered from the atmosphere over (potentially) geologic timescales. We found that sediment burial in the valley (topset) was more than twice the sediment export flux to the lake (bottomset). As our measurements of fluvial deposits and previous lake sediment data (Geirsdóttir et al., 2009) show broadly similar OC concentrations, the difference in sediment flux implies that most of the CO_2 sequestration by OC since deglaciation was driven by terrestrial sediment burial in the delta topset as oppose to export to the delta bottom set.

The greater C sink associated with the growth of the valley sediment fill (i.e., topset deposition) may be underappreciated as much research on the long-term implications of the terrestrial OC cycle has highlighted only the riverine export fluxes of OC (Galy et al., 2015; Hilton, 2017) despite existing evidence for large floodplain reservoirs of OC (Cierjacks et al., 2010; Hoffmann et al., 2009; Lininger et al., 2019; Sutfin et al., 2016; Sutfin & Wohl, 2017; Wohl et al., 2012, 2017). Both lateral migration and vertical aggradation are common to low-sloping river systems (Dunne & Aalto, 2013; Muto & Steel, 1992), which highlights the potential application of these dynamics to terrestrial systems elsewhere in the global OC cycle over a wide range of timescales. Similarly, the formation and subsequent filling of overdeepened valleys, as observed at our study site, is common to all glaciated systems (Alley et al., 1999) and likely has important C cycle implications (Smith et al., 2015), especially during interglacial periods.

The dynamics of sediment storage and entrainment in fluvial systems can render suspended sediments and fluvial deposits as two complementary, but distinct OC pools. So, without constraining the inventories and compositions of both OC pools, it is not possible to fully constrain terrestrial OC cycle dynamics (Figure 12). Moreover, our results suggest that estimates of the climate dependence of OC cycling rates can only be fully determined after assessing the effects of sediment storage with independent measurements (as discussed in Torres et al., 2017).

Because the storage of OC in floodplains sequesters CO_2 from the atmosphere, the dynamics represented in the Efri Haukadalsá River catchment illustrate an emerging link between the transient storage of OC and Earth's climate. Given the large size of the OC reservoir, the long tail of its age distribution, and the ability of rivers to rapidly respond to climatic change, the storage of OC in floodplains may serve as an important capacitor in the carbon cycle that sequesters and ages carbon during periods of slow lateral migration and/or aggradation, while releasing aged carbon during periods of rapid lateral migration and/or incision.

Acknowledgments
This work was supported by a grant from the Caltech Discovery Fund to W. W. F. and M. P. L. and Caltech CEMI (W. W. F.). M. A. T. acknowledges support from the Caltech Texaco Postdoctoral Fellowship and the California Alliance for Graduate Education & The Professoriate. P. C. K. acknowledges support from the Fannie and John Hertz Foundation, Cohan/Jacobs and Stein Families Fellowship, and the DoD, Air Force Office of Scientific Research, National Defense Science and Engineering Graduate (NDSEG) Fellowship, 32 CFR 168a. Portions of this research were carried out at the Stanford Synchrotron Radiation Lightsource, a Directorate of SLAC National Accelerator Laboratory and an Office of Science User Facility operated for the US Department of Energy Office of Science by Stanford University. We acknowledge DEMs provided by the Polar Geospatial Center under NSF OPP Awards 1043681, 1559691, and 1542736. All authors thank Dr. A. Joshua West for the loaning of equipment, as well as Dr. S. Webb for assistance at SLAC beamline 14-3. The use of the EPMA facility at the Department of Earth Science, Rice University, Houston, TX, is kindly acknowledged along with the assistance of Dr. Gelu Costin. The geochemical data produced as part of this study are available online (at doi.org/10.1594/PANGAEA.911027). The data analysis codes are available online (at github.com/torres-lab) and archived (at https://doi.org/10.5281/zenodo.3688815).

References

Abbott, M. B., & Stafford, T. W. (1996). Radiocarbon geochemistry of modern and ancient Arctic lake systems, Baffin Island, Canada. *Quaternary Research*, *45*(3), 300–311.

Alley, R. B., Strasser, J. C., Lawson, D. E., Evenson, E. B., & Larson, G. J. (1999). Glaciological and geological implications of basal-ice accretion in overdeepenings. *Glacial Processes Past and Present*. Boulder, CO: Geological Society of America.

Arnalds, O. (2004). Volcanic soils of Iceland. *Catena*, *56*(1-3), 3–20.

Bao, R., McNichol, A. P., Hemingway, J. D., Gaylord, M. C. L., & Eglinton, T. I. (2019). Influence of different acid treatments on the radiocarbon content spectrum of sedimentary organic matter determined by RPO/Accelerator Mass Spectrometry. *Radiocarbon*, *61*(2), 395–413.

Blöthe, J. H., & Korup, O. (2013). Millennial lag times in the Himalayan sediment routing system. *Earth and Planetary Science Letters*, *382*, 38–46.

Bolin, B., & Rodhe, H. (1973). A note on the concepts of age distribution and transit time in natural reservoirs. *Tellus*, *25*(1), 58–62.

Bouchez, J., Beyssac, O., & Galy, V. (2010). Oxidation of petrogenic organic carbon in the Amazon floodplain as a source of atmospheric CO2. *Geology*, *38*(3), 255–258.

Bradley, D. N., & Tucker, G. E. (2013). The storage time, age, and erosion hazard of laterally accreted sediment on the floodplain of a simulated meandering river. *Journal of Geophysical Research: Earth Surface*, *118*, 1308–1319. https://doi.org/10.1002/jgrf.20083

Brock, F., Froese, D. G., & Roberts, R. G. (2010). Low temperature (LT) combustion of sediments does not necessarily provide accurate radiocarbon ages for site chronology. *Quaternary Geochronology*, *5*(6), 625–630.

Ciais, P., Tagliabue, A., Cuntz, M., Bopp, L., Scholze, M., Hoffmann, G., et al. (2012). Large inert carbon pool in the terrestrial biosphere during the Last Glacial Maximum. *Nature Geoscience*, *5*(1), 74–79.

Cierjacks, A., Kleinschmit, B., Babinsky, M., Kleinschroth, F., Markert, A., Menzel, M., et al. (2010). Carbon stocks of soil and vegetation on Danubian floodplains. *Journal of Plant Nutrition and Soil Science*, *173*(5), 644–653.

Constantine, J. A., Dunne, T., Ahmed, J., Legleiter, C., & Eli, D. (2014). Sediment supply as a driver of river evolution in the Amazon Basin. *Nature Geoscience*, *7*, 899–903.

Doetterl, S., Berhe, A. A., Nadeu, E., Wang, Z., Sommer, M., & Fiener, P. (2016). Erosion, deposition and soil carbon: A review of process-level controls, experimental tools and models to address C cycling in dynamic landscapes. *Earth-Science Reviews*, *154*, 102–122.

Dosseto, A., Bourdon, B., Gaillardet, J., Maurice-Bourgoin, L., & Allegre, C. J. (2006). Weathering and transport of sediments in the Bolivian Andes: Time constraints from uranium-series isotopes. *Earth and Planetary Science Letters*, *248*(3-4), 759–771.

Douglas, P. M. J., Pagani, M., Eglinton, T. I., Brenner, M., Hodell, D. A., Curtis, J. H., et al. (2014). Pre-aged plant waxes in tropical lake sediments and their influence on the chronology of molecular paleoclimate proxy records. *Geochimica et Cosmochimica Acta*, *141*, 346–364.

Dunne, T., & Aalto, R. E. (2013). *Large River Floodplains* (Vol. 9). San Diego, CA: Elsevier.

France-Lanord, C., & Derry, L. A. (1997). Organic carbon burial forcing of the carbon cycle from Himalayan erosion. *Nature*, *390*(6655), 65–67.

French, K. L., Hein, C. J., Haghipour, N., Wacker, L., Kudrass, H. R., Eglinton, T. I., & Galy, V. (2018). Millennial soil retention of terrestrial organic matter deposited in the Bengal Fan. *Scientific Reports*, *8*(1), 11997.

Galy, V., Beyssac, O., France-Lanord, C., & Eglinton, T. (2008). Recycling of graphite during Himalayan erosion: A geological stabilization of carbon in the crust. *Science*, *322*(5903), 943–945.

Galy, V., & Eglinton, T. (2011). Protracted storage of biospheric carbon in the Ganges–Brahmaputra basin. *Nature Geoscience*, *4*(12), 843–847.

Galy, V., Peucker-Ehrenbrink, B., & Eglinton, T. (2015). Global carbon export from the terrestrial biosphere controlled by erosion. *Nature*, *521*(7551), 204–207.

Ganti, V., Straub, K. M., Foufoula-Georgiou, E., & Paola, C. (2011). Space-time dynamics of depositional systems: Experimental evidence and theoretical modeling of heavy-tailed statistics. *Journal of Geophysical Research*, *116*, F02011. https://doi.org/10.1029/2010JF001893

Geirsdóttir, Á., Miller, G. H., Thordarson, T., & Ólafsdóttir, K. (2009). A 2000 year record of climate variations reconstructed from Haukadalsvatn, West Iceland. *Journal of Paleolimnology*, *41*(1), 95–115.

Gislason, S. R., Oelkers, E. H., Eiriksdottir, E. S., Kardjilov, M. I., Gisladottir, G., Sigfusson, B., et al. (2009). Direct evidence of the feedback between climate and weathering. *Earth and Planetary Science Letters*, *277*(1–2), 213–222.

Granet, M., Chabaux, F., Stille, P., Dosseto, a., France-Lanord, C., & Blaes, E. (2010). U-series disequilibria in suspended river sediments and implication for sediment transfer time in alluvial plains: The case of the Himalayan rivers. *Geochimica et Cosmochimica Acta*, *74*(10), 2851–2865.

Grönvold, K., Óskarsson, N., Johnsen, S. J., Clausen, H. B., Hammer, C. U., Bond, G., & Bard, E. (1995). Ash layers from Iceland in the Greenland GRIP ice core correlated with oceanic and land sediments. *Earth and Planetary Science Letters*, *135*(1–4), 149–155.

He, Y., Trumbore, S. E., Torn, M. S., Harden, J. W., Vaughn, L. J. S., Allison, S. D., & Randerson, J. T. (2016). Radiocarbon constraints imply reduced carbon uptake by soils during the 21st century. *Science (New York, N.Y.)*, *353*(6306), 1419–1424.

Hemingway, J. D., Rothman, D. H., Grant, K. E., Rosengard, S. Z., Eglinton, T. I., Derry, L. A., & Galy, V. V. (2019). Mineral protection regulates long-term global preservation of natural organic carbon. *Nature*, *570*(7760), 228.

Hilton, R. G. (2017). Climate regulates the erosional carbon export from the terrestrial biosphere. *Geomorphology*, *277*, 118–132.

Hoffmann, T., Glatzel, S., & Dikau, R. (2009). A carbon storage perspective on alluvial sediment storage in the Rhine catchment. *Geomorphology*, *108*(1–2), 127–137.

Howard, A. D., & Knutson, T. R. (1984). Sufficient conditions for river meandering: A simulation approach. *Water Resources Research*, *20*(11), 1659–1667.

Jalilehvand, F. (2005). Sulfur speciation in intact plant leaves by XANES spectroscopy. In Saito, K. (Ed.), *Sulfur transport and assimilation in plants in the post genomic era* (pp. 53–57). Leiden, The Netherlands: Backhuys Publishers.

James, L. A. (1996). Polynomial and power functions for glacial valley cross-section morphology. *Earth Surface Processes and Landforms*, *21*(5), 413–432.

Jenny, H., Gessel, S. P., & Bingham, F. T. (1949). Comparative study of decomposition rates of organic matter in temperate and tropical regions. *Soil Science*, *68*(6), 419–432.

Keeling, C. D. (1960). The concentration and isotopic abundances of carbon dioxide in the atmosphere. *Tellus*, *12*(2), 200–203.

Keeling, R. F., & Shertz, S. R. (1992). Seasonal and interannual variations in atmospheric oxygen and implications for the global carbon cycle. *Nature*, *358*(6389), 723–727.

Kennedy, M. J., Pevear, D. R., & Hill, R. J. (2002). Mineral surface control of organic carbon in black shale. *Science*, *295*(5555), 657–660.

Lalonde, K., Mucci, A., Ouellet, A., & Gélinas, Y. (2012). Preservation of organic matter in sediments promoted by iron. *Nature*, *483*(7388), 198.

Lauer, J. W., & Parker, G. (2008). Modeling framework for sediment deposition, storage, and evacuation in the floodplain of a meandering river: Theory. *Water Resources Research*, *44*, W04425. https://doi.org/10.1029/2006WR005528

Lawrence, C. R., Harden, J. W., Xu, X., Schulz, M. S., & Trumbore, S. E. (2015). Long-term controls on soil organic carbon with depth and time: A case study from the Cowlitz River Chronosequence, WA USA. *Geoderma*, *247-248*, 73–87.

Li, C., Yang, S., xin Zhao, J., Dosseto, A., Bi, L., & Clark, T. R. (2016). The time scale of river sediment source-to-sink processes in East Asia. *Chemical Geology*, *446*, 138–146.

Limaye, A. B. S., & Lamb, M. P. (2013). A vector-based method for bank-material tracking in coupled models of meandering and landscape evolution. *Journal of Geophysical Research: Earth Surface*, *118*, 2421–2437. https://doi.org/10.1002/2013JF002854

Lininger, K., Wohl, E., Rose, J., & Leisz, S. J. (2019). Significant floodplain soil organic carbon storage along a large high-latitude river and its tributaries. *Geophysical Research Letters*, *46*, 2121–2129. https://doi.org/10.1029/2018GL080996

Lougheed, B., & Obrochta, S. (2016). MatCal: Open source Bayesian ^{14}C age calibration in Matlab. *Journal of Open Research Software*, *4*(1), e42.

Malmon, D. V., Dunne, T., Reneau, S. L., The, S., & September, N. (2003). Stochastic theory of particle trajectories through alluvial valley floors. *The Journal of Geology*, *111*(5), 525–542.

Manceau, A., & Nagy, K. L. (2012). Quantitative analysis of sulfur functional groups in natural organic matter by XANES spectroscopy. *Geochimica et Cosmochimica Acta*, *99*, 206–223.

Martin, E. E., Ingalls, A. E., Richey, J. E., Keil, R. G., Santos, G. M., Truxal, L. T., et al. (2013). Age of riverine carbon suggests rapid export of terrestrial primary production in tropics. *Geophysical Research Letters*, *40*, 5687–5691. https://doi.org/10.1002/2013GL057450

Martin, C. W., & Johnson, W. C. (1995). Variation in radiocarbon ages of soil organic matter fractions from late Quaternary buried soils. *Quaternary Research*, *43*(2), 232–237.

Masiello, C. A., & Druffel, E. R. M. (2001). Carbon isotope geochemistry of the Santa Clara River. *Global Biogeochemical Cycles*, *15*(2), 407–416.

Mayer, L. M. (1994). Surface area control of organic carbon accumulation in continental shelf sediments. *Geochimica et Cosmochimica Acta*, *58*(4), 1271–1284.

McGeehin, J., Burr, G. S., Jull, A. T., Reines, D., Gosse, J., Davis, P., et al. (2001). Stepped-combustion ^{14}C dating of sediment: A comparison with established techniques. *Radiocarbon*, *43*(2A), 255–261.

Mehegan, J. M., Robinson, P. T., & Delaney, J. R. (1982). Secondary mineralization and hydrothermal alteration in the Reydarfjordur drill core, eastern Iceland. *Journal of Geophysical Research*, *87*(B8), 6511–6524.

Mey, J., Scherler, D., Zeilinger, G., & Strecker, M. R. (2015). Estimating the fill thickness and bedrock topography in intermontane valleys using artificial neural networks. *Journal of Geophysical Research: Earth Surface*, *120*, 1301–1320. https://doi.org/10.1002/2014JF003270

Middelburg, J. J. (1989). A simple rate model for organic matter decomposition in marine sediments. *Geochimica et Cosmochimica Acta*, *53*(7), 1577–1581.

Muehlenbachs, K., Anderson Jr, A. T., & Sigvaldason, G. E. (1974). Low-O18 basalts from Iceland. *Geochimica et Cosmochimica Acta*, *38*(4), 577–588.

Muto, T., & Steel, R. J. (1992). Retreat of the front in a prograding delta. *Geology*, *20*(11), 967–970.

Neteler, M., Bowman, M., Landa, M., & Metz, M. (2012). GRASS GIS: A multi-purpose open source GIS. *Environmental Modelling & Software*, *31*, 124–130. https://doi.org/10.1016/j.envsoft.2011.11.014

Ólafsson, G. (1998). Eiríksstaðir í haukadal: Fornleifarannsókn á skálarúst.

Otto, J.-C., Schrott, L., Jaboyedoff, M., & Dikau, R. (2009). Quantifying sediment storage in a high alpine valley (Turtmanntal, Switzerland). *Earth Surface Processes and Landforms: The Journal of the British Geomorphological Research Group*, *34*(13), 1726–1742.

Pachauri, R. K., Allen, M. R., Barros, V. R., Broome, J., Cramer, W., Christ, R., et al. (2014). Climate change 2014: Synthesis report. In Pachauri, R., & Meyer, L (Eds.), *Contribution of Working Groups I, II and III to the Fifth Assessment Report of the Intergovernmental Panel on Climate Change* (pp. 151). Geneva, Switzerland: IPCC.

Pickering, I. J., George, G. N., Yu, E. Y., Brune, D. C., Tuschak, C., Overmann, J., et al. (2001). Analysis of sulfur biochemistry of sulfur bacteria using X-ray absorption spectroscopy. *Biochemistry*, *40*(27), 8138–8145.

Pizzuto, J., Keeler, J., Skalak, K., & Karwan, D. (2017). Storage filters upland suspended sediment signals delivered from watersheds. *Geology*, *44*(2), G38170.1.

Porter, C., Morin, P., Howat, I., Noh, M.-J., Bates, B., Peterman, K., et al. (2018). Arcticdem. https://doi.org/10.7910/DVN/OHHUKH

Poulin, B. A., Ryan, J. N., Nagy, K. L., Stubbins, A., Dittmar, T., Orem, W., et al. (2017). Spatial dependence of reduced sulfur in Everglades dissolved organic matter controlled by sulfate enrichment. *Environmental Science & Technology*, *51*(7), 3630–3639.

Raich, J. W., & Schlesinger, W. H. (1992). The global carbon dioxide flux in soil respiration and its relationship to vegetation and climate. *Tellus B*, *44*(2), 81–99.

Sadler, P. M. (1981). Sediment accumulation rates and the completeness of stratigraphic sections. *The Journal of Geology*, *89*(5), 569–584.

Schmidt, M. W. I., Torn, M. S., Abiven, S., Dittmar, T., Guggenberger, G., Janssens, I. A., et al. (2011). Persistence of soil organic matter as an ecosystem property. *Nature*, *478*, 49–56.

Schroth, A. W., Bostick, B. C., Graham, M., Kaste, J. M., Mitchell, M. J., & Friedland, A. J. (2007). Sulfur species behavior in soil organic matter during decomposition. *Journal of Geophysical Research*, *112*, G04011. https://doi.org/10.1029/2007JG000538

Schwenk, J., Khandelwal, A., Fratkin, M., Kumar, V., & Foufoula-Georgiou, E. (2017). High spatiotemporal resolution of river planform dynamics from Landsat: The RivMAP toolbox and results from the Ucayali River. *Earth and Space Science*, *4*(2), 46–75.

Smith, R. W., Bianchi, T. S., Allison, M., Savage, C., & Galy, V. (2015). High rates of organic carbon burial in fjord sediments globally. *Nature Geoscience*, *8*(6), 450.

Stallard, R. F. (1998). Terrestrial sedimentation and the carbon cycle: Coupling weathering and erosion to carbon burial. *Global Biogeochemical Cycles*, *12*(2), 231–257.

Sutfin, N. A., & Wohl, E. (2017). Substantial soil organic carbon retention along floodplains of mountain streams. *Journal of Geophysical Research: Earth Surface*, *122*, 1325–1338. https://doi.org/10.1002/2016JF004004

Sutfin, N. A., Wohl, E. E., & Dwire, K. A. (2016). Banking carbon: A review of organic carbon storage and physical factors influencing retention in floodplains and riparian ecosystems. *Earth Surface Processes and Landforms*, *41*(1), 38–60.

Tao, S., Eglinton, T. I., Montluçon, D. B., McIntyre, C., & Zhao, M. (2015). Pre-aged soil organic carbon as a major component of the Yellow River suspended load: Regional significance and global relevance. *Earth and Planetary Science Letters*, *414*, 77–86.

Torn, M. S., Trumbore, S. E., Chadwick, O. a., Vitousek, P. M., & Hendricks, D. M. (1997). Mineral control of soil organic carbon storage and turnover. *Nature*, *389*(1992), 3601–3603.

Torres, M. A., Limaye, A. B., Ganti, V., Lamb, M. P., West, A. J., & Fischer, W. W. (2017). Model predictions of long-lived storage of organic carbon in river deposits. *Earth Surface Dynamics*, *5*(4), 711.

Turowski, J. M., Hilton, R. G., & Sparkes, R. (2016). Decadal carbon discharge by a mountain stream is dominated by coarse organic matter. *Geology*, *44*(1), 27–30.

Wittmann, H., von Blanckenburg, F., Dannhaus, N., Bouchez, J., Gaillardet, J., Guyot, J. L., et al. (2015). A test of the cosmogenic ^{10}Be(meteoric)/^{9}Be proxy for simultaneously determining basin-wide erosion rates, denudation rates, and the degree of weathering in the Amazon basin. *Journal of Geophysical Research: Earth Surface*, *120*, 2498–2526. https://doi.org/10.1002/2015JF003581

Wohl, E., Dwire, K., Sutfin, N., Polvi, L., & Bazan, R. (2012). Mechanisms of carbon storage in mountainous headwater rivers. *Nature Communications*, *3*, 1263.

Wohl, E., Hall Jr, R. O., Lininger, K. B., Sutfin, N. A., & Walters, D. M. (2017). Carbon dynamics of river corridors and the effects of human alterations. *Ecological Monographs*, *87*(3), 379–409.

Wolfe, A. P., Miller, G. H., Olsen, C. A., Forman, S. L., Doran, P. T., & Holmgren, S. U. (2004). Geochronology of high latitude lake sediments. In *Long-term environmental change in Arctic and Antarctic lakes* (pp. 19–52). Dordrecht, The Netherlands: Springer.

Zhu, M. X., Chen, L. J., Yang, G. P., Huang, X. L., & Zhao, Y. D. (2016). Composition of organic sulfur in riverine and marine sediments: Insights from sulfur stable isotopes and XANES spectroscopy. *Organic Geochemistry*, *99*, 102–112.